MASS-TRANSFER CORRELATIONS FOR THE DUAL BED COLLOIDAL SUSPENSION REACTOR

A Thesis

Presented to

The Academic Faculty

By

Rajiv Jaini

In Partial Fulfillment

of the Requirements for the Degree

Master of Science in Chemical Engineering in the

School of Chemical and Biomolecular Engineering

Georgia Institute of Technology

August 2013

MASS-TRANSFER CORRELATIONS FOR THE DUAL BED COLLOIDAL SUSPENSION REACTOR

Approved by:

Dr. Thomas F. Fuller, Advisor

School of Chemical & Biomolecular Engineering

Georgia Institute of Technology

Dr. William Koros

School of Chemical & Biomolecular Engineering

Georgia Institute of Technology

Dr. Paul Kohl

School of Chemical & Biomolecular Engineering

Georgia Institute of Technology

Date Approved: May 17, 2013

ACKNOWLEDGEMENTS

I would like to thank Professor Fuller for his support. I would also like to thank Brad Parker and Jeff Andrews for helping me build the diffusion cells used in this work. I would also like to thank SunCatalytix for sponsoring this project. I would like to thank my family for their support through this process as well.

Table of Contents

LIST OF TABLES

LIST OF FIGURES

LIST OF ABBREVIATIONS AND SYMBOLS

PEC	Photoelectrochemical
DBCSR	Dual Bed Colloidal Suspension Reactor
A_c	cross sectional area for diffusion, m^2
A_{ch}	cross sectional area (length, width) of the channel, m^2
Ar*	Modified Archimedes number
c	concentration, $mol \times m^{-3}$
$c_{1,i}$	concentration in left cell, species i, $mol \times m^{-3}$
$c_{2,i}$	concentration in right cell, species i , $mol \times m^{-3}$
$c_{A,i}$	initial concentration of species A, $mol \times m^{-3}$
c_i	concentration of species i, $mol \times m^{-3}$
$c_{LB,i}$	concentration of species i in left bulk solution, $mol \times m^{-3}$
$c_{RB,i}$	concentration of species i in right bulk solution, $mol \times m^{-3}$
D	diffusion coefficient, $m^2 \times s^{-1}$
d_{ch}	depth of channel, m

$D_{eff,i}$	effective diffusivity of species *i*, $m^2 \times s^{-1}$
δ	stagnant layer thickness, m
d_o	orifice diameter, mm
E_e	solar irradiance, $W \times m^{-2}$
$\varepsilon_{\text{sparge}}$	diffusion cell sparging void fraction
ε_{tot}	diffusion cell void fraction
$\varepsilon_{\text{tube}}$	diffusion cell tube void fraction
Fractional Loss	parasitic loss due to pumping
g	gravity, $m \times s^{-2}$
G	integration constant
$G^o_{H_2}$	standard Gibbs Free Energy change on combusting hydrogen gas, $kJ \times kmol^{-1}$
G^o	standard Gibbs Free Energy change, $kJ \times kmol^{-1}$
H^o	standard enthalpy change, $kJ \times kmol^{-1}$
k_c	overall mass-transfer coefficient, $m \times s^{-1}$

k_i	integration constant
$k_{L,i}$	left channel mass-transfer coefficient of species *i*, $m \times s^{-1}$
$k_{M,i}$	membrane mass-transfer coefficient of species *i*, $m \times s^{-1}$
$K_{OV,i}$	overall mass-transfer coefficient of species *i*, $m \times s^{-1}$
$k_{R,i}$	right channel mass-transfer coefficient of species *i*, $m \times s^{-1}$
L	Buckingham π length, m
L_{ch}	length of channel, m
LHV_{H_2}	lower heating value of hydrogen gas, $kW\text{-}hr \times kg_{H_2}^{-1}$
M	Buckingham π mass, kg
MW_{H_2}	molecular weight of hydrogen gas, $g \times mol^{-1}$
μ	liquid viscosity
$\bar{\mu}$	mean
$\vec{N}_i$	flux of species *i*
n_{H_2}	moles of hydrogen, kmol

n	number of variables
N_o	number of orifices
η_{STH}	solar to hydrogen conversion efficiency
P_{H_2}	daily production rate of hydrogen, $kg \times day^{-1}$
π	Buckingham π dimensionless groups
Ψ	psi, dimensionless constant
r	rank of dimensionless matrix
Re	Reynolds number
R_{H_2}	rate of hydrogen gas formation, $mol \times m^{-3} \times s^{-1}$
ρ	density, $kg \times m^{-3}$
ρ_l	density of liquid, $kg \times m^{-3}$
ρ_g	density of gas, $kg \times m^{-3}$
R_i	reaction rate of species *i*, $mol \times m^{-3} \times s^{-1}$
RSE	relative standard error, %
Sc	Schmidt number

Sh	Sherwood number
S^o	standard change in entropy, $kJ \times kmol^{-1} \times K^{-1}$
σ	standard deviation
t	Buckingham π time
t	time, mins
θ_i	dimensionless concentration of species *i*
u	substitution constant
V_{air}	volumetric flow rate in the channel, $L \times min^{-1}$
V_{evap}	diffusion cell evaporation rate, $L \times min^{-1}$
v_g	measured gas velocity, $m \times s^{-1}$
$V_{out,bubble}$	diffusion cell bubble saturation rate, $L \times min^{-1}$
v_{sg}	superficial gas velocity, $m \times s^{-1}$
$\dot{V}$	volumetric flow rate, $L \times min^{-1}$
$V_{tot,lost}$	total evaporation rate, $L \times min^{-1}$

w_{cell}	width of the cell, m
w_{ch}	channel width, m
$\overline{x}$	dimensionless length

SUMMARY

To meet the growing energy world demands, and in conjunction, lower CO_2 production levels, near zero emission energy sources must be pushed to the forefront as alternatives to fossil fuels. Photoelectrochemical (PEC) cells are a potential alternative to fossil fuels and have recently generated much interest because of their potential to electrolyze water into hydrogen fuel from sunlight. But in order to be competitive with fossil fuels, understanding the mass-transfer limitations in PEC systems is critical. This work focuses on the addressing the mass-transfer limitations in a conceptually novel PEC cell reactor, the Dual Bed Colloidal Suspension Reactor (DBCSR).

Mass-transfer correlations for the DBCSR are presented. The correlations are based on experimental data obtained using two fabricated diffusion cells. The working correlation representative of both cells is

$$\mathrm{Sh} = 0.009\mathrm{Re}^{0.386}\mathrm{Ar}^{*0.250}\,\mathrm{Sc}^{0.333}\left(\frac{w_{ch}}{d_o}\right)^{1.182}\varepsilon^{0.116}.$$

An analysis of the orientation of the gas sparger suggests that the transport phenomena in both cells is not the same, and therefore using two correlations to represent similar systems is justified. An energy analysis is presented that shows that gas sparging is a low energy consumption option to mitigate mass-transfer limitations. Future work is suggested for better understanding the mass-transfer behavior in the DBCSR.

CHAPTER 1

INTRODUCTION

1.1 Energy Challenges and Renewable Requirements

Recently, concerns over a growing world population and improved standards of living have led to an increased discussion in energy resources and the impact of current energy practices on the environment. In, 2011, the World Bank estimated the World's Population to be around 7 billion people. The United Nations has reported that by the middle of the century, the world's population is expected to reach 9.3 billion people [1]. The population growth, coupled with increased standards of living, will require an increase in the world's energy supply. In 2001, the world's energy usage was approximately 13.5 TW. Expectations are that by the middle of the century, the world's energy usage is expected to double to approximately 27 TW [2, 3]. As Lewis et al. explains, enough fossil fuel energy reserves are available to supply the demands of an expanding population, but the associated carbon dioxide (CO_2) by-product of burning fossil fuels is expected have an unknown, but adverse, impact on the global environment. Additionally, despite factoring enhancements in carbon capturing technologies, expectations remain that the overall CO_2 production levels are to increase by almost double their current levels [3]. To meet the growing energy world demands, and in conjunction, lower CO_2 production levels, near zero emission energy sources must be pushed to the forefront as alternatives to fossil fuels for both transportation and stationary power requirements. Several requirements must be met in order for a perspective energy source to be considered a potential fossil fuel alternative. Potential alternatives should be both economically viable with fossil fuels and environmentally less hazardous than fossil fuels. The fuels should also be produced in large

enough amounts such that they influence energy supply markets. And finally, the fuels should output more energy than is required to produce them [4].

1.2 Transportation and Stationary Power

Energy consumption can be subdivided into two categories: transportation and stationary power. Transportation is currently dominated by petroleum derived liquid fuels. Rechargeable batteries, fuel cells, and biofuels are possible energy sources that have potential to displace petroleum based liquid fuels. Rechargeable batteries, particularly, lithium-ion based batteries, show much promise in displacing current liquid fuels because of their potential implementation in hybrid electric or all electric vehicles. However, research is needed to address lithium-ion battery performance and to reduce production costs [5]. Fuel cells, like batteries, show potential to be used in the transportation sector. Yet, high costs currently dominate the industry and research must be done to find more effective ways to supply and store hydrogen [6]. Biofuels also show promise in displacing current liquid fuels. Examples of biofuels include fuels derived from crops, like ethanol, and fuels derived from plant matter, like algae. However, as with lithium-ion batteries, energy yields must increase and production costs must be lowered in order to displace the incumbents in a market dominated by petroleum based liquid fuels [2, 4].

Stationary power is currently dominated by coal for the purposes of electricity production. Wind, nuclear energy, and solar energy are renewable energy sources that have potential to displace coal. Wind as a stationary power source shows promise as an electricity source, but issues regarding converting wind turbine motion to electricity at the generator need to be addressed for a larger scaled implementation [7]. Nuclear energy has been widely used in the past, generating around 14% of the world's electrical power. However, inherent safety concerns

and issues with disposal of waste still need to be studied [2]. Solar fuel sources are typically subdivided into fuels from solar thermal energy and fuels generated from the utilization of semiconducting materials [8]. Solar thermal energy is based on concentrating sunlight in an effort to convert sunlight into heat that can be used to heat fluids. Engineering better materials to withstand the elevated temperatures associated with solar thermal processes is required for larger scale implementation [2, 9]. Semiconducting materials are used as materials for photovoltaics, which convert sunlight to electricity. Photoelectrochemical (PEC) cells also use semiconducting materials and have recently generated much interest because of their potential to electrolyze water into hydrogen fuel from sunlight. Graetzel refers to this as the "highly prized goal of photoelectrochemical research" [10, 11]. Currently, between the two, photovoltaics dominate the solar fuels industry [2]. As with other electrical power generating processes, there are two issues preventing PEC cells from seriously competing with not only fossil fuels but also photovoltaics [3]. The first impediment in the competitive use of PEC devices is their relatively high costs compared to energy produced from fossil fuels. The high costs are primarily the result of inefficiencies in the conversion of sunlight to electricity generation process [10-12]. The second impediment in the competitive use of PEC devices is the safety of the generated product. An artificial photosynthetic system appears to be a promising idea for the storage of solar fuels, particularly in the design of PEC cells. These cells allow for water splitting to occur in the presence of light to form hydrogen and oxygen gases. This means that captured solar energy is stored in the bonds of a chemical, in this case hydrogen [3]. However, additional issues exist with such a system. Hydrogen and oxygen are both produced simultaneously from the same location and as a result can form a combustible mixture. This combination poses safety

concerns. However, these safety concerns are addressed with the proposal of the Dual Bed Colloidal Suspension Reactor (DBCSR) [13].

1.3 The Dual Bed Colloidal Suspension Reactor

The DBCSR is a PEC cell reactor designed to electrolyze water with the intent of safely converting solar energy to chemical fuels. A schematic of the reactor is shown in Figure 1. The DBCSR is composed of two channels, two types of colloidal photocatalysts, electrolyte solution capable of carrying charge, a membrane separator, and a thin plastic film designed to capture product gases. The two channels are separated by a porous membrane, which allows for the conduction of ions and neutral molecules. The two channels contain distinct colloidal photocatalysts suspended in liquid water. In each of the channels, separate oxidation and reduction reactions occur that allow for the generation of hydrogen gas in one channel and oxygen gas in the other channel. At one photocatalyst, the oxidation reaction is

$$4A + 2H_2O \xrightarrow{h\nu} 4H^+ + 4B^- + O_2 . \quad (1)$$

At the other photocatalyst, the reduction reaction is

$$4H^+ + 4B^- \xrightarrow{h\nu} 2H_2 + 4A . \quad (2)$$

A and B are species that transport charge from one channel to the other channel. These charge carrying species are present in the solution in the channels. These species serve as the electronic charge carriers that transport between the two channels to keep an overall charge balance in the reactor. Species that serve as electron carriers are commonly referred to as redox

shuttles or redox mediators [14]. An example of a redox mediator is the iodide, triiodide I^-, I_3^- couple [15].

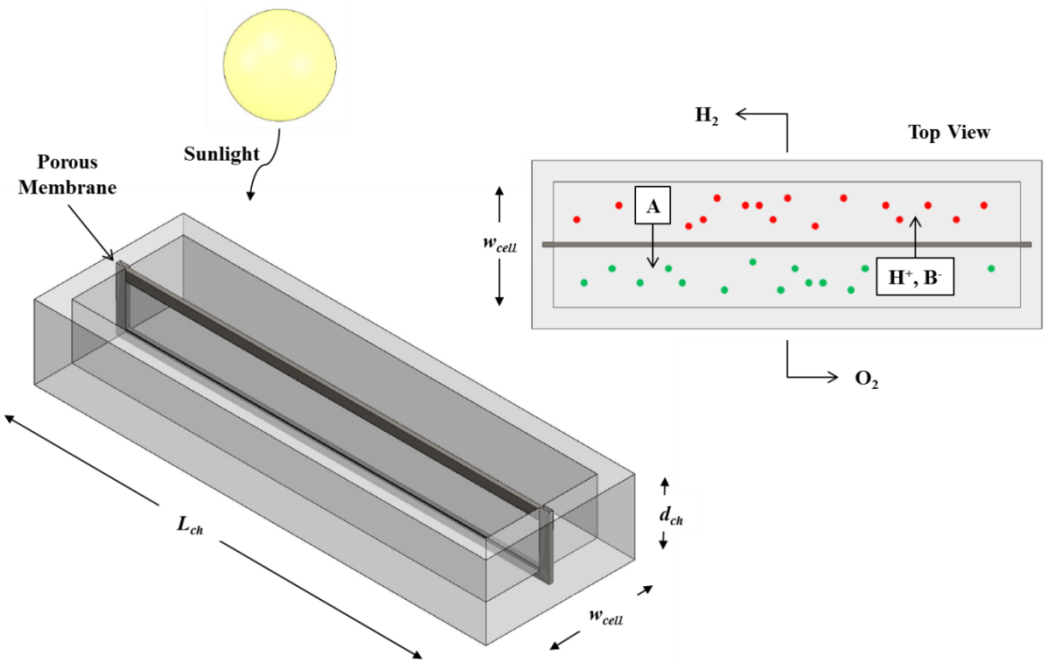

Figure 1. A schematic of the Dual Bed Colloidal Suspension Reactor. Source: Adapted from James et al. [13].

The reactor channels are separated by a porous membrane. The porous membrane acts as a separator, separating the hydrogen and oxygen products, separating the colloidal catalysts, but allowing the transport of the redox mediator between both channels. A thin plastic film covers the tops of each of the channels to collect the produced gases. The film is transparent and allows the passage of photons. Additionally, because the channels are contained, the hydrogen and oxygen gases produced upon reaction are captured by the plastic film, which is able to expand or contract based on the amount of gas produced. And because of the transparent plastic film that

covers the channels, light passes and allows the reaction to proceed, but evaporation of water into the air is mitigated.

After the water splitting proceeds in one channel, charged species are transported through the membrane to the adjacent channel. The membrane is placed at least at the height of the solution in the channels. The membrane is selected so that the resistance to transport is low. Dissolved gases are expected to diffuse from one channel to another. An efficiency loss from this crossover of dissolved gases can be estimated, assuming knowledge of the separator area.

1.4 Modeling the Transport

A one dimensional, steady-state diffusion reaction model is constructed to understand better the transport occurring in the system. In this model, molecular diffusion alone accounts for the transport of the redox mediating species (i.e., A forms B) from channel to channel. The following assumptions are made in the model:

1) The channel length and channel depth are fixed and are independent considerations not included in the model. The length is ignored because it is assumed to be long enough that end effects are negligible. The channel depth is controlled by the penetration of sunlight into the solution, which is a consequence of the design. Hence, obtaining a channel width is the focus of the model. Figure 2 shows the dimensions of the reactor.

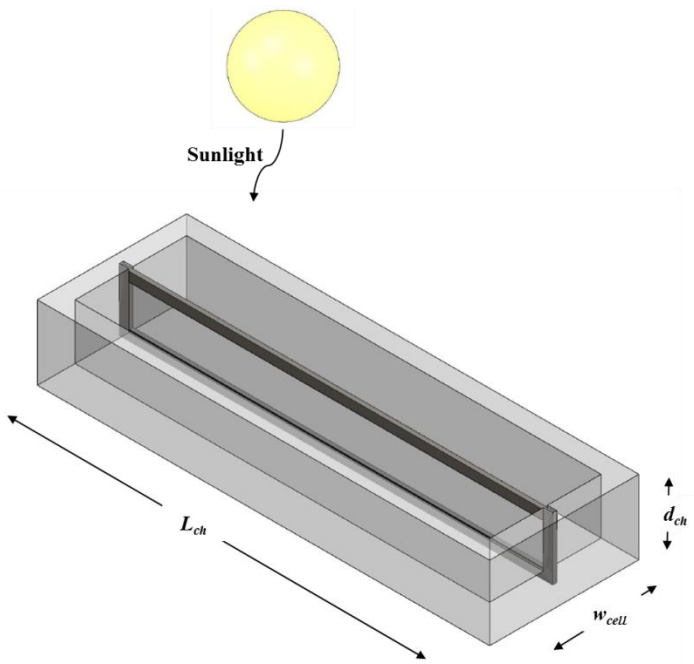

Figure 2. The dimensions of the DBCSR are labeled as a reference to the model.

2) The liquid phases in the model are stagnant fluids. A liquid phase diffusion coefficient of 10^{-9} $m^2 \times s^{-1}$ is assumed.

3) The homogeneous zero-order reaction rate for the production of H_2(g) is calculated based on assumptions about efficiencies and expected solar irradiance. That is,

$$R_{H_2} = \frac{\eta_{STH} E_e}{LHV_{H_2} MW_{H_2} d_{ch}} \tag{3}$$

where R_{H_2} is the generation rate of H_2(g), η_{STH} is the solar to hydrogen conversion efficiency, E_e is the solar irradiance, LHV_{H_2} is the lower heating value of H_2(g), MW_{H_2} is the molecular weight of H_2(g), and d_{ch} is the depth of the channel. Values for the parameters are shown in Table 1.

Table 1. Parameters used in analytic model.

Parameter	Value	Units
η_{STH}	0.1	--
E_e	1	$kW \times m^{-2}$
LHV_{H_2} [16]	33	$kW\text{-}hr \times kg_{H_2}^{-1}$
MW_{H_2}	2	$g \times mol^{-1}$
d_{ch}	0.1	m
R_{H_2}	0.00421	$(mol\ H_2) \times m^{-3} \times s^{-1}$

4) No reaction occurs in the membrane.

5) The modeled reaction is similar to the concept of a redox mediator. A reacts to form B in one channel and B reacts to form A in the other channel. Because the rate of the conversion of A to B is limited to the rate of hydrogen generation reaction, both rate constants are equal. That is $R_{H_2} = R_A$.

6) Because the membrane thickness is unknown, the membrane is assumed to be one percent of the reactor width. This value is selected based on knowledge of the results of the model.

The derivation, including the final steady-state equations used to model the dimensionless concentration profile, is included in Appendix A. In the membrane, the differential equation describing the dimensionless concentration, θ, as a function of dimensionless distance, $\bar{x}$, is

$$\frac{\partial^2 \theta}{\partial \overline{x}^2} = 0 \,. \tag{4}$$

In the liquid phase, the differential equation describing the dimensionless concentration, θ, as a function of dimensionless distance, $\overline{x}$, is

$$\frac{\partial^2 \theta}{\partial \overline{x}^2} = -\frac{w_{ch}^2 R_A}{c_{A,i} D_A} = \Psi \tag{5}$$

where w_{ch} is the channel width, $c_{A,i}$ is the initial concentration A, D_A is the diffusivity of species A, and Ψ is a dimensionless constant, which is dimensionless. Knowing the value of Ψ allows one to determine potential channel widths as

$$w_{ch} = \left(\frac{\Psi c_{A,i} D_A}{R_A} \right)^{\frac{1}{2}} . \tag{6}$$

Figure 3 shows the dimensionless concentration profile along the width of the reactor for various values of Ψ. A dimensionless length of 0 implies that the species is at the center of the membrane. A dimensionless length of 1 or -1 implies that the species is at the walls of the reactor.

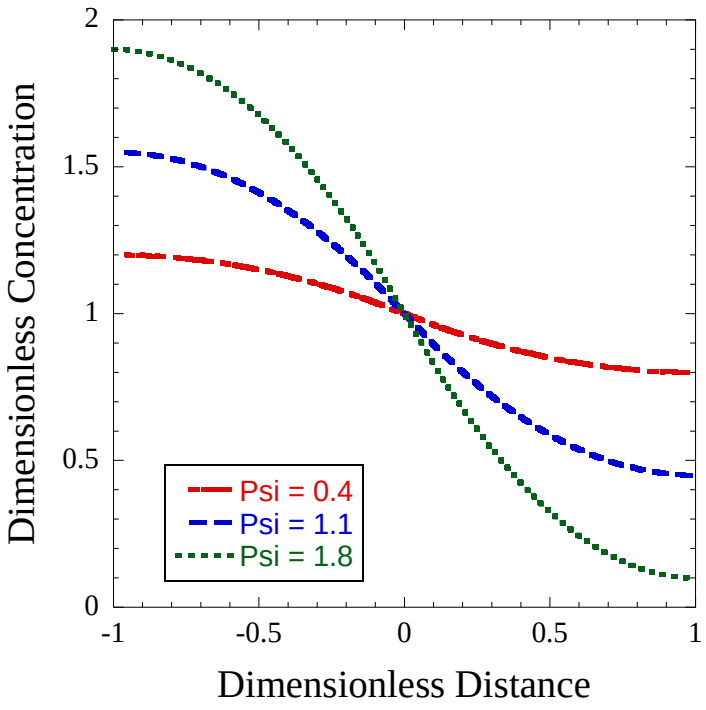

Figure 3. A plot of the dimensionless concentration profile along the width of the reactor assuming a redox mediator type of reactor. The concentration of species A is only shown.

In the limiting case of zero kinetics, represented by a dimensionless concentration of 1, the concentration of A in the system is uniform everywhere in the reactor. In the case of fast kinetics, the concentration A approaches zero at the end of the right channel away from the separator. A limiting concentration of A is assumed to be 10% of the equilibrium concentration of species A. Hence, a value of 1.8 for Ψ is selected to model the width of the channel assuming a stagnant fluid in the channels.

As shown in equation 3, the channel width is determined to be proportional to the square root of Ψ, and upon conversion, the channel width is found to be on the order of millimeters. The results are shown in Table 2.

Table 2. Modeling parameters and results.

Parameter	Value	Units
$c_{A,i}$	1000	M
D_A	10^{-9}	$m^2 \times s^{-1}$
R_A	0.00421	$mol \times m^{-3} \times s^{-1}$
w_{ch}	20.7	m

The results of the model suggest that the maximum channel width is around 20.7 mm, with respect to the other input parameters. This result suggests that for the input parameters shown, A is exhausted by the point the channel width is 20.7 mm. This means that for any reactor width over 20.7 mm, the reactor is oversized, and any size larger than the maximum size means unused reactor space. Effectively, the reactor is mass-transfer limited. Assuming a $1{,}000\ kg \times day^{-1}$ production rate of hydrogen gas [13], an approximate calculation of the reactor length shows that the reactor length required is unreasonably long. That is,

$$P_{H_2} = R_{H_2} V_{ch} t \tag{7}$$

where P_{H_2} is the daily production rate of hydrogen, at $1{,}000\ kg \times day^{-1}$, R_{H_2} is the rate constant at which hydrogen is formed (previously given), V_{ch} is the volume of the channel, and t is the time in seconds over which the reactor runs, which is equivalent to twenty-four hours. Because the channel width, 20.7 mm, and the channel depth, 10 cm are known, the length of the channel is determined to be

$$L_{ch} = \frac{P_{H_2}}{d_{ch} w_{ch} R_{H_2} t}. \quad (8)$$

Solving for L_{ch} gives an approximate channel length of 664 km, assuming a 1,000 kg×day^{-1} production rate. The material costs resulting from building excessively thin and long reactors like the one that the model suggests are likely to be higher than building a wider, less long reactor. In order to reduce the length assuming the daily production target, either the channel width or the channel depth need to be increased. Because the channel depth is fixed by the optimal penetration depth of sunlight, the channel width is determined to be the only parameter that can be increased.

CHAPTER 2

METHODS TO ENHANCE MASS TRANSFER

2.1 Motivation of Mass Transfer Enhancement

There are two motivating factors to enhance the mass transfer in the DBCSR. The first factor results from the mass-transfer analysis in Chapter 1. That is, the reactor channel width is mass-transfer limited. As can be imagined, mass-transfer rates must be increased in order to mitigate the mass-transfer limitation. For example, if the reactor width was infinitely long, infinitely fast mass transfer would be needed to satisfy reactions occurring in the channels. Therefore, any increase in the reactor width must be accompanied with an increase in mass-transfer rates. Second, an increase in the reactor width requires that the reactor must be fully utilized. If the reaction occurs only near the membrane, then increasing the reactor width adds no benefit, as photocatalyst far from the membrane is not utilized. In order to address both of these issues, this work proposes gas sparging the solution in the channels to enhance mass-transfer and promote channel uniformity. Gas sparging is expected to increase the rate of mass-transfer, so as to allow the channels to be sized considerably wider than the mass-transfer limited reaction diffusion model suggests. Additionally, by introducing gas into the solution, a well-mixed bulk phase is expected to form, promoting the uniformity in the solution and increasing reactor utilization. Figure 4 provides an illustration of the gas sparging flow path. In the figure, the product gas is shown to recycle through the channels after being pumped to an adequate pressure.

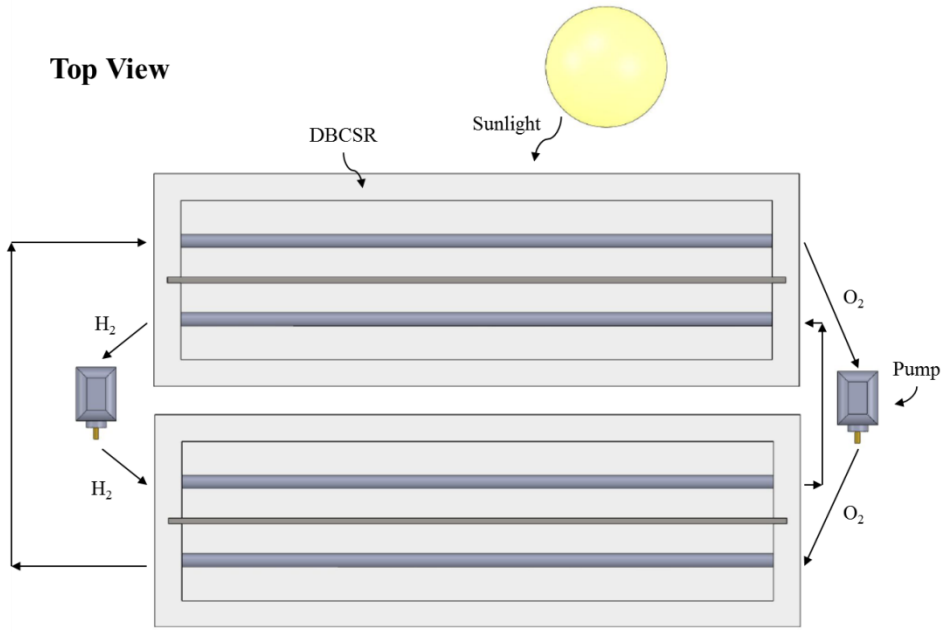

Figure 4. Gas sparging illustration in which product gas is recirculated through a pump into the channels.

The following sections are meant to discuss how gas sparging reduces diffusion lengths and thereby increase mass-transfer rates, discuss how utilization increases result from gas sparging, provide examples of the role of gas sparging in other applications, and give some physical insight into gas sparging with a discussion of bubble formation in liquid solutions.

2.2 Mass-Transfer Rate Increases Resulting from Gas Sparging

A channel level view of the DBCSR in operation incorporating gas sparging is shown in Figure 5. The schematic shows the transport of species A across the channel, eventually forming B. In the first step, A leaves the stagnant fluid of the adjacent channel, traverses across the separator (membrane), and enters the stagnant fluid of the oxygen gas producing channel. In the second step, A then leaves the stagnant fluid and mixes into the bulk phase approaching the

photocatalyst surface. A reaches the surface of the photocatalyst after leaving the bulk phase and diffusing through the photocatalyst boundary layer, at which point oxygen gas is generated. In the third step, B leaves the surface of the photocatalyst, passes through the boundary layer, and then B reenters the stagnant fluid region of the channel, traverses the separator, and exits the channel in the fourth step. At this point, B forms A through the same steps in the other channel (not shown). The sparged gas is shown as a swarm of bubbles. If the sparged gas is not present, then the stagnant fluid region occupies the entire channel. In this stagnant fluid region, only diffusion occurs. Therefore, the rate of production of oxygen gas is limited by the rate at which diffusion brings A to the surface of the photocatalyst in this stagnant layer region. But, because of the mixing effect induced by gas sparging the solution, the stagnant layer thickness is reduced. That is, the stagnant layer in which diffusion occurs only occupies a region near the separator. Hence, the rate of mass transfer is increased by reducing the thickness of the stagnant layer.

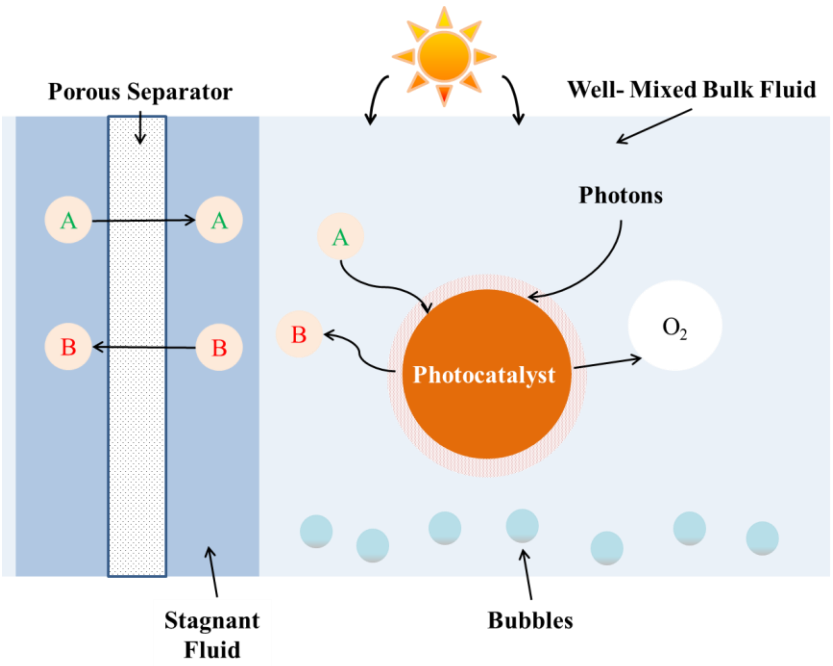

Figure 5. A simplified view is shown of the process in which gases are produced at the photocatalyst surface.

2.3 Utilization Increases Resulting from Gas Sparging

Figure 6 is an illustration that emphasizes the impact of non-uniformity (a) versus uniformity (b) in the channels. In Figure 6a, species A is seen transporting towards the photocatalyst, and upon reaction, leaves the surface reduced as negatively charged species B. The schematic shows that non-uniformity in the solution is the cause of clustering of species A at or near the separator. This leaves the photocatalysts further from the separator unused and causes mass-transfer limitations in the channel. In Figure 6b, species A is again seen transporting towards the photocatalyst surface, and again upon reaction, leaving the surface reduced as negatively charged species B. However, in schematic Figure 6b the uniformity of the solution is the cause of the reaction occurring throughout the entire channel width. That is, the clustering seen in Figure 6a is reduced, allowing more photocatalysts to be used. This uniformity increases photocatalyst utilization. By gas sparging the channel solution, a well-mixed bulk fluid region is expected to form, with the implication that the concentration in this region is uniform, as seen in Figure 5. This means that in a scenario like that seen in Figure 6b, the rate of production of gases is no longer mass-transfer limited as it is in Figure 6a.

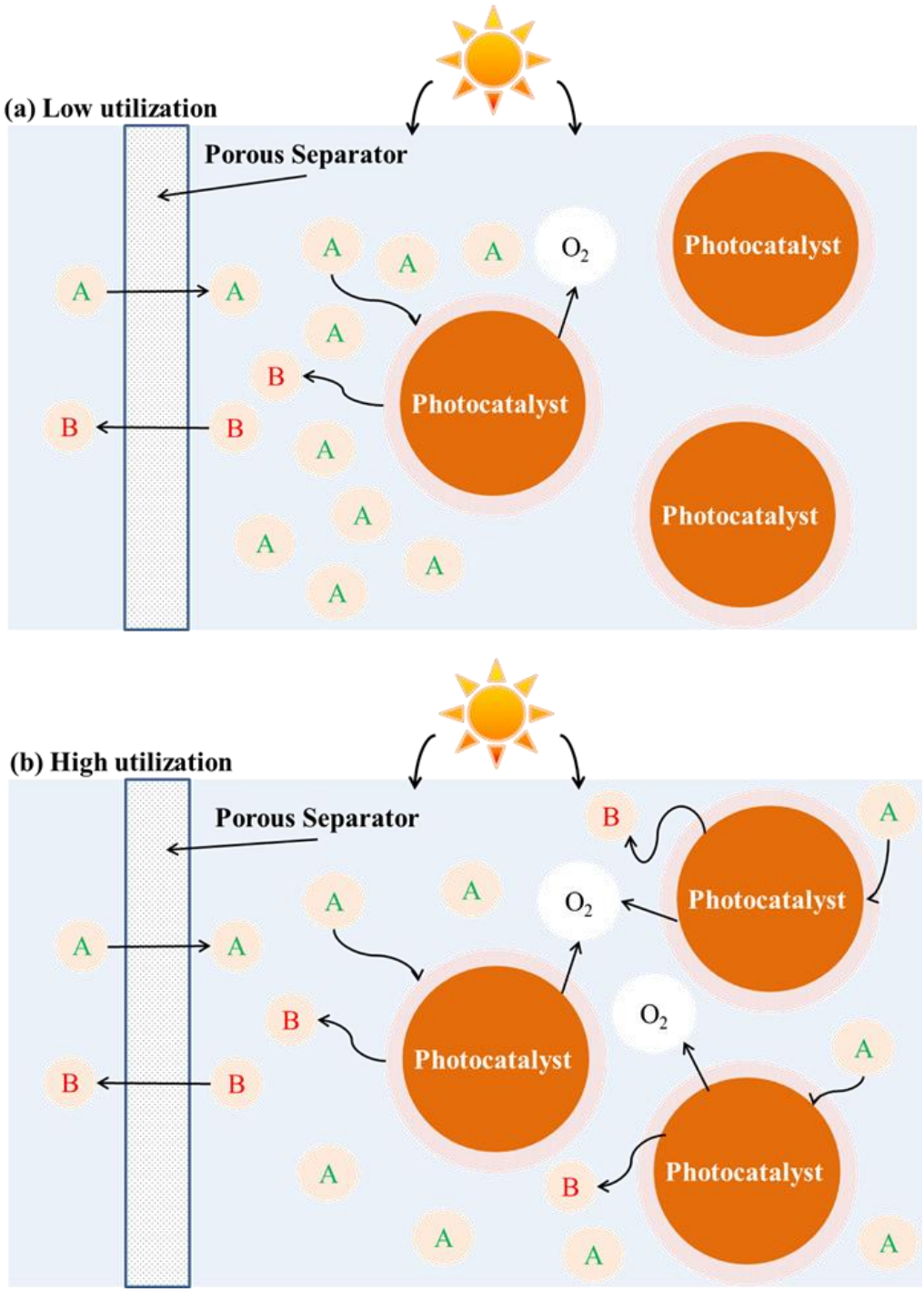

Figure 6. The effect of non-uniformity is compared. In (a), the non-uniformity of the solution limits the reaction to only a subset of the channel, reducing the overall efficiency. In (b), the solution concentration is more uniform, allowing for more utilization of the reactor channel.

2.4 Gas Sparging in Other Applications

In systems where increased mixing is a requirement, gas sparging typically serves as an effective, low energy alternative to mechanical agitation [17]. In many applications, mass-transfer rates are limited by diffusion rates in stagnant fluids. Agitating a fluid extensively enhances mass transfer by reducing diffusion distances, which can be described as a thinning of the stagnant concentration layer adjacent to a stagnant solid body. Many industrial applications can benefit or already benefit from the of use gas sparging as a mass-transfer enhancing mechanism [18]. Electroplating and electropolishing are typical applications that can be enhanced by introducing gas sparging [17]. In electropolishing, sometimes thought of as the reverse of plating, metal surfaces are smoothed by electrochemical removal of some of the metal. Sehdamed et al. have studied the effects of gas sparging on electropolishing. In their work, the group notes that electropolishing applications are limited to diffusion rates from the surface of the metal to the bulk solution. The transport rate of impurities from the surface is enhanced by agitating the electrolytic fluid, thereby reducing the stagnant layer thickness by the electrode [17]. Gas liquid contacting is another industrial application using gas sparging. Mass transfer is enhanced in this two-phase region, where the liquid and bubble make contact. In low viscosity solutions, mechanical stirring can be circumvented in place of gas sparging [19]. Botton et. al show that for specific bubble column designs mechanical agitation is actually less effective than sparging [20]. In other electrochemical applications, the correlation of gas sparging and bubble behavior to dimensionless expressions for mass transfer has been the focus of several studies for electrowinning. Gas sparging in such systems has been routinely used and is known to enhance mass transfer at gas-evolving electrodes [21]. Haque et al. report the results of using variable sparger designs in an attempt to study flow patterns and bubble formation [22]. Gas sparging has

also been applied to systems requiring microfiltration and ultrafiltration, aiding in enhancing permeate concentration [23]. Mechanisms for mass transfer at gas evolving electrodes have also been reported [21, 22, 24]. Sigrist et al. report mass-transfer coefficients for electrowinning cells that utilize gas sparging [24, 25]. As the literature suggests, gas sparging provides substantial benefit in enhancing mass transfer in other applications.

2.5 Bubble Convection and Flux Enhancement

In the DBCSR, sparged gas flow rates enhance the transport from channel to channel. But, the behavior depends on more than just the gas flow rate in the reactor. This enhancement effect also depends on the bubbles introduced into the system by the sparging action. The convection caused by rising bubbles in fluids has been studied in other systems, and analogies are drawn from those systems that apply to the DBCSR.

A literature review shows that bubble convection, bubble size, bubble formation, and hydrodynamic conditions caused by bubbles are critical in both enhancing and understanding the mass-transfer behavior of the system being studied. The effect of bubble convection is seen extensively in both gas-evolving electrodes and electrowinning systems. Two of the main areas studied in mass-transfer controlled processes are subsets of hydrodynamics. That is, free and forced convection. Free convection, when mixing occurs as a result of density differences, has been noted to have significant effects on the flux enhancement in other systems. Forced convection, when mechanical agitation causes mixing, at gas evolving electrodes has also increased understanding of bubble behavior in sparging systems [21, 23, 26]. Bubble formation at gas evolving electrodes has improved the understanding of the effects of void fraction and bubble velocity on mass transfer occurring in electrochemical systems [27]. Miller et al. have

reported that mass transfer is a function of mean bubble size. Understanding the effect of bubble size has allowed the development of scale-up procedures in electrowinning cells [28]. Bubble size studies are commonly employed in bioreactor designs, in an effort to increase mass transfer from the gas to the liquid phases. Bredwell et al. have reported the enhancement of mass transfer by introducing microbubbles, bubbles orders of magnitude smaller than those found in typical bioreactors, to enhance mass transfer by increasing gas to liquid contact area [29]. The desire to understand bubble formation has also led to studying the dynamics of bubble coalescence and break up, which can intuitively have a large effect on the mixing within the system. Prince et al. have developed a model that predicts not only coalescing and break up rates but also equilibrium bubble size in a gas-liquid type contactor [30]. As noted by Cabassud et al., the flow pattern and thus the hydrodynamic conditions near a flowing fluid-wall interface are effected by the rate of gas sparging and void fraction in the system [31].

The studies of the literature, bubble convection, size, formation, and hydrodynamics, are all applicable to understanding the mass transfer in the DBCSR. The effect of bubble convection is important in the DBCSR primarily because of the requirements for effective mixing and increasing flux. The mixing effect, which is also a function of bubble size, allows the reactor to be sized more realistically. The bubble size and characteristics are a function of the orifice size used. Additionally, the hydrodynamics of fluid flow are critical in sizing the reactor, because of the stagnant layer resistance thin film model. That is, by thinning the stagnant layer of fluid adjacent to the membrane, mass transfer resistance decreases, and subsequently, flux increases. As explained in the later chapters, fabricated diffusion cells conceptually based on the design of the DBCSR are used to understand the hydrodynamic behavior, specifically the convection patterns that are formed within each channel via gas sparging.

CHAPTER 3

DEVELOPING A MASS-TRANSFER CORRELATION

3.1 Mass Transfer Analysis

The primary focus of this work is to quantify mass transfer in the DBCSR. One method is to relate the flux to diffusion occurring in the system. This can be done by using Fick's First Law of Diffusion. Fick's Law states that the diffusive flux in a system is proportional to the concentration gradient applied on the system,

$$\vec{N}_i = -D_i \nabla c_i \tag{1}$$

and that matter goes from areas of high concentrations to low concentrations, neglecting the effect of mass transfer by convection, where $\vec{N}_i$ is the flux of species *i*, D_i is the diffusion coefficient of species *i*, and c_i is the concentration of species *i*. A detailed mass-transfer analysis of a system is obtained by combining Fick's Law with a material balance on fixed points within the system. Generally, the material balance is written in the form of

$$\frac{\partial c_i}{\partial t} = -\nabla \cdot \vec{N}_i + R_i \tag{2}$$

where c_i is the concentration of species *i*, $\vec{N}_i$ is the flux of species *i*, and R_i is a homogeneous reaction rate at which species *i* is formed or consumed. These two equations, coupled with a known set of boundary and initial conditions, allow one to obtain both a concentration profile and flux across the two points. In many cases, a detailed mass-transfer analysis which provides information about both a concentration profile and flux across boundaries is either practical or

needed. For example, steady-state diffusion across a thin film in which the concentration on one side of the film is higher than the other side is not a mathematically intensive problem to solve using Fick's Law.

But, some cases are not as easily described using Fick's Law. Mass transfer across boundaries is an example, where hydrodynamics cause velocity fields. In such systems, velocity profiles are nearly impossible to obtain, as convective mass transfer must be included in any calculations. In cases like these, it remains simpler to express the mass transfer using a proportionality constant that incorporates the design of the system. In these systems, the bulk phase concentrations are used as the driving force. This proportionality constant that relates the flux of material to concentration differences is typically referred to as a mass-transfer coefficient. The representation of mass transfer in this sort of system is written as

$$N = k_c(c_1 - c_2) \tag{3}$$

where N is the flux between bulk concentrations, k_c is the mass-transfer coefficient, and c_1 and c_2 are concentrations, either at interfaces or in bulk solutions.

Unlike Fick's Law, this definition of the flux relies on knowing measureable bulk phase concentrations, as the gradient in concentration is replaced by a concentration difference. The mass-transfer coefficient has dimensions of length per unit time.

The goal of this work is to obtain a mass-transfer coefficient for a unique reactor design. The mass-transfer coefficient approach is chosen because the design of the system facilitates the

use of mass-transfer coefficients for the reasons mentioned previously. An illustration of a lab scale reactor is shown in Figure 7.

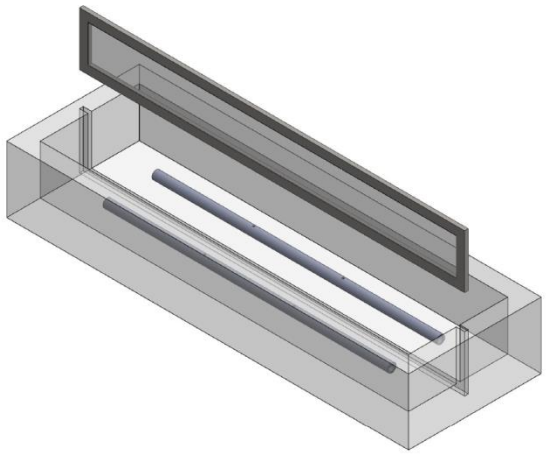

Figure 7. An illustration of the reactor design described by a mass-transfer coefficient.

In this design, two fluid bearing channels are separated by a membrane to allow the transport of solute particles to and from bulk phases. Additionally, gas sparging is used in the channels to keep the solutions well mixed for purposes that are required by the application. A stagnant layer of unknown thickness develops in the channels as a result of the sparging. In consequence, it becomes quite difficult to describe the mass transfer using Fick's Law, and in convenience, the mass transfer of the system is described using the second approach, a mass-transfer coefficient [32-35].

3.2 Film Theory

After determining that mass transfer is best described by a mass-transfer coefficient, potential models describing the physical situation are sifted through to better understand the mass transfer process [32]. This work makes use of concepts theorized by Nernst to describe

mass transfer occurring at an interface. Nernst developed film theory, which assumed that an unstirred layer of fluid exists near every interface. This unstirred layer of fluid is commonly referred to as a stagnant film as seen in Figure 8.

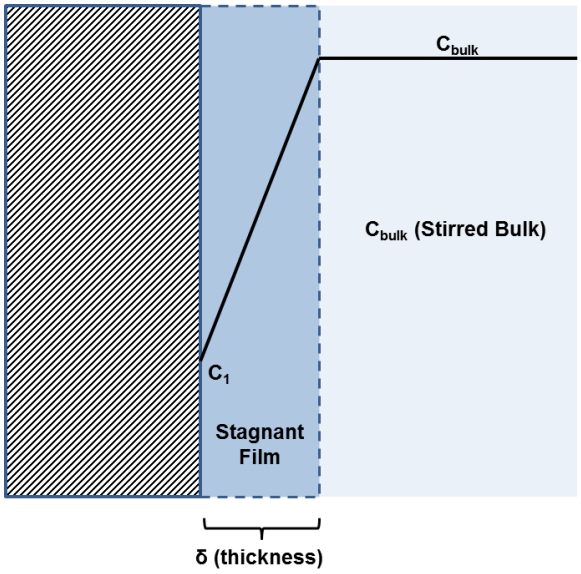

Figure 8. An illustration of the stagnant film concept.

It is here that the largest changes in concentration are assumed to occur. And hence, the solution resistance to mass transfer is also determined by the thickness of this layer. The immediate consequence of film theory is that even though mass transfer through the stagnant layer is occurring by a combination of convection and diffusion, mass transfer can be described both in terms of the diffusion coefficient and the mass-transfer coefficient. Using Figure 8 as a model of film theory, one sees that

$$N = k_c(c_{bulk} - c_1) = \frac{D}{\delta}(c_{bulk} - c_1) \tag{4}$$

can be used to express the mass transfer relative to the interface, where δ is the film thickness, c_{bulk} is the bulk concentration, and c_1 is a measureable concentration beyond the interface. Additionally, the mass-transfer coefficient is rewritten in terms of diffusion and stagnant film thickness by combining the expressions to show that

$$k_c = \frac{D}{\delta} \tag{5}$$

Rearranging, one finds that a direct consequence of film theory is the Sherwood number dimensionless group. That is,

$$\mathrm{Sh} = \frac{k_c \delta}{D}. \tag{6}$$

This dimensionless group, the Sherwood number, is conveniently rewritten as a function of other common dimensionless groups that are significant to the system. These functions are typically referred to as mass-transfer correlations, and one is derived for the specific geometry found in this work [32-35].

3.3 The Lumped Parameter Model Solution

Film theory makes use of a stagnant fluid model in which the largest changes in concentration occur within the film that is used to describe the resistance to mass transfer. This theory can be used to quantify the solution resistance, and in turn, the individual mass-transfer coefficients. The model that describes this process is referred to as the "Lumped Parameter Model" [32]. For example, in the DBCSR, based on the implication of the thin film model, three resistances exist. The resistances are shown in Figure 9.

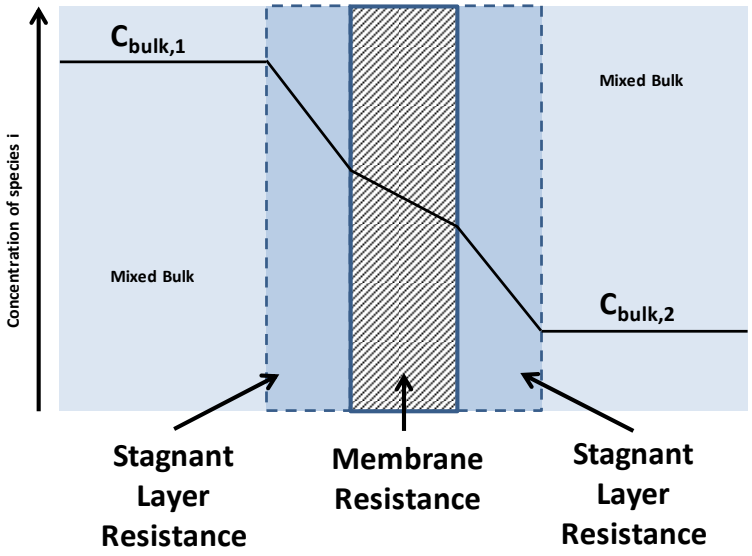

Figure 9. Series resistances are listed for the reactor. The resistances in the thin films that are adjacent to the membrane are shown as stagnant layer resistances. The resistance in the membrane is shown as a membrane resistance. The lumped parameter model, a consequence of using film theory, is used to determine the value of the individual resistances.

The two resistances at the solution membrane interface are represented by thin films. The membrane resistance is lumped in between these resistances. Using the thin film model requires that concentrations are measureable. In this case, the concentration at or in the membrane is not measureable. The only measureable concentrations are the two bulk phase concentrations. In result, the mass-transfer coefficient from channel to channel is determined by applying the expression

$$N_i = K_{ov,i}\left(c_{LB,i} - c_{RB,i}\right), \tag{7}$$

where $c_{LB,i}$ is the bulk phase concentration $c_{bulk,1}$ in the schematic, and $c_{RB,i}$ is the bulk phase concentration $c_{bulk,2}$ in the schematic. The expression can be rewritten to represent the mass-transfer coefficient as a resistance. The total resistance is expressed as

$$N_i = \frac{c_{LB,i} - c_{RB,i}}{\frac{1}{K_{ov,i}}} \tag{8}$$

where $K_{ov,i}^{-1}$ is the total resistance from bulk phase to bulk phase. The derivation of this expression is shown in Appendix D. The resistances are expressed in series as

$$\frac{1}{k_{L,i}} + \frac{1}{k_{M,i}} + \frac{1}{k_{R,i}} = \frac{1}{K_{ov,i}} \tag{9}$$

where $\frac{1}{k_{L,i}}$ is the resistance in the left channel, $\frac{1}{k_{M,i}}$ is the resistance in the membrane, and $\frac{1}{k_{R,i}}$ is the resistance in the right channel. The resistance in the membrane is determined by measuring the diffusion coefficient in the membrane. The expression for the membrane resistance is

$$\frac{1}{k_{M,i}} = \frac{\delta}{D_{eff,i}} \tag{10}$$

where $D_{eff,i}$ is the effective diffusivity of species *i* and δ is the thickness of the filter paper. If the conditions are identical on both sides of the membrane, then the channel mass-transfer resistances are

$$\frac{1}{K_{ov,i}} - \frac{1}{k_{M,i}} = \frac{1}{k_{L,i}} + \frac{1}{k_{R,i}} = \frac{2}{k_{ch}} \tag{11}$$

where k_{ch} is the channel mass-transfer coefficient. The channel mass-transfer coefficient is obtained by experimental methods, which is discussed in detail in the following sections.

3.4 Dimensionless Correlations

Upon being able to express all of the resistances by the lumped parameter model solution, the mass-transfer coefficient is rewritten as a correlation based on system properties. Dimensionless correlations offer a unique perspective at examining physical ratios and measuring their relative magnitudes. For example, in the case of the Schmidt number, Sc, the common interpretation allows one to quantify the ratio of the thicknesses of hydrodynamic boundary layer to the concentration boundary layer. Additionally, these correlations reduce the number of experiments required to understand the system mass transfer. Instead of varying many sets of individual parameters and measuring the impact of the parameter on mass-transfer coefficient individually, a lesser number of parameters can be changed, and their impact quantified in terms of common dimensionless groups. That ability of dimensionless groups, like the Schmidt number, to tell physical information about the system, like the ratio of the thicknesses of layers, is helpful when trying to predict system behavior from available data. Hence, dimensionless correlations are a valuable asset in engineering applications, and coincidentally, exist in many parts of the available literature.

A literature review of commonly reported dimensionless correlations has led to the understanding that a universal correlation does not exist that describes mass transfer for all such

types of systems. However, most correlations are based on some sort of physical design in which mass transfer or heat transfer is of concern. And those correlations have been reported based on the experimental results associated with the particular systems. Dimensional analysis has led to the representation of a primary dimensionless group, the Sherwood number [32, 33]. In many cases, mass transfer for the system is described using a modified Sherwood number, with functionality based on other dimensionless groups [27, 36]. Rates of mass transfer have also been represented by the Stanton number [37, 38]. Chao et al. report dimensionless models that include the effect of volatile organic compounds and suspended particles on mass transfer [36]. Stephan et al. have theorized and compared mass transfer at gas evolving electrodes to experimental data. These dimensionless models correlating mass transfer from a spherical bubble next to a wall have been confirmed against experimental data [39]. Khamadieva et al. have also proposed mass-transfer models represented by the Stanton and Sherwood dimensionless groups. These expressions are developed with an emphasis being placed on understanding the role of the liquid viscosity in the system [40]. Hosny et al. report results on the enhancement of the mass-transfer coefficient in gas sparged zinc electrolytic systems. A correlation using the Sherwood, Schmidt, and Reynolds dimensionless groups is presented in their work [41, 42]. Vogt reports a theoretical dimensionless correlation, confirmed by experimental results, in a gas electrode forming system that accounts for temperature gradients in combination with concentration gradients in the liquid electrolyte boundary layer [21, 43]. As a result, one is to expect some error associated with mass-transfer correlations [44]. This error is a result of the combination of the empirical nature of the correlation and any associated experimental error. Furthermore, the correlation is only as precise as the assumptions that go into it. But, these engineering correlations provide as an effective way, with respect to the error

associated with them, of understanding the physical characteristics of a system and how the independent parameters in the system affect one another. Despite the previous work on similar systems, there is no correlation in the literature that corresponds closely to the DBCSR with gas sparging. Consequently, the objective of this work is to develop a correlation suitable for the design and scale up of these systems.

3.5 Derivation of the Correlation

One of the goals of this work is to obtain a mass-transfer correlation, like those in the literature, for the DBCSR. A simplified reactor geometry, like that shown in Figure 7, is assumed to be representative of the geometry of the DBCSR. A detailed description of the geometry, as well as the components is given in Chapter 4. In developing the functional form of the mass-transfer correlation, the Buckingham π theorem is used. This theorem requires first identifying the important physical variables in the system. Then, after assigning numerical values to the dimensions of each group, a set of core variables from the physical variables is chosen. This group of core variables forms the core of each dimensionless group used to describe the system. The remaining physical variables are individually combined with the core variables to obtain the final functional form.

Table 3. List of variables for Buckingham π.

Variable Group	Physical Variable Name	Symbol	Dimensions
1	Diffusivity	D	$L^2 \times t^{-1}$
2	Channel Width	w_{ch}	L
3	Density Difference between Liquid and Gas	$\Delta\rho = (\rho_l - \rho_g)$	$M \times L^3$
	Liquid Density	ρ_l	$M \times L^3$
	Gas Density	ρ_g	$M \times L^3$
4	Mass-Transfer Coefficient	k_{ch}	$L \times t^{-1}$
5	Liquid Viscosity	μ	$M \times (Lt)^{-1}$
6	Gravity	g	$L \times t^{-2}$
7	Orifice Diameter	d_o	L
8	Gas Velocity	v_g	$L \times t^{-1}$
9	Superficial Gas Velocity	v_{sg}	$L \times t^{-1}$

For this particular geometry, nine physical variables are used to describe the system. The variables are shown in Table 3. The commonality amongst these parameters is their ability to be measured. The nine parameters are listed, along with their numbering, in the left most columns of the table. Their symbols are listed in the third column, along with their physical dimensions in the fourth column. The parameters are not an exhaustive list. Rather, they are chosen to best represent the system, based on intuition on the process. That is, this method is not based on scientific principle but still serves as an effective tool in developing a correlation.

Table 4. Physical variables and dimensions.

Dimensions	Physical Variable								
	D	w_{ch}	ρ_l, ρ_g, $\Delta\rho$	k_{ch}	μ	g	d_o	v_g	v_{sg}
M	0	0	1	0	1	0	0	0	0
L	2	1	-3	1	-1	1	1	1	1
t	-1	0	0	1	-1	-2	0	1	1

Table 4 shows how the physical variables relate to the independent physical dimensions in the system, where 'M' represents mass, 'L' represents length, and 't' represents time. These core, physically independent dimensions, are assigned a specific numerical value to the physical variable based on the dimensions shown. For example, because diffusivity has dimensions of squared length per unit time, and no physical dependence on mass, the diffusivity column in Table 4, contains zero units for mass, two units for length, and negative one units for time. Values that are negative represent values found in the denominator.

After determining the dimensions of the physical variables, the number of dimensionless groups is determined to be the remainder of the difference between the number of variables and the dimensional matrix. This value is often referred to as 'π' [32]. That is,

$$\text{Dimensionless Groups} = \text{Number of Variables} - \text{Rank of Dimensional Matrix} \tag{12}$$

$$\pi = n - r \tag{13}$$

$$6 = 9 - 3 \tag{14}$$

$$\therefore 1 = f(\pi_1\pi_2\pi_3\pi_4\pi_5\pi_6) \tag{15}$$

where n is the number of dimensionless group and r is the rank of the matrix. In results, there are 6 dimensionless groups required. The selected core variables to be in each dimensionless group are

$$D, w_{ch}, \Delta\rho\,. \tag{16}$$

The remaining six variables to be used to compose each of the six dimensionless groups are

$$k_{ch}, \mu, g, d_o, v_g, v_{sg}\,. \tag{17}$$

As shown in Appendix B, using the core variables, in combination with the six other physical variables, the Buckingham Pi theorem results in a correlation of the form

$$\mathrm{Sh} = f(\mathrm{Re}, \mathrm{Ar}^*, \mathrm{Sc}, \frac{d_o}{w_{ch}}, \varepsilon) \tag{18}$$

where Sh represents the Sherwood number, Sc represents the Schmidt number, Ar* represents the modified Archimedes number, $\frac{d_o}{w_{ch}}$ is the ratio of the orifice diameter to the channel width, Re is the Reynolds number, and ε epsilon represents the ratio of gas to liquid volume in the channel during an experiment.

Table 5. Definition of dimensionless groups.

Variable	Definition	Interpretation
Sh	$\frac{k_{ch} w_{ch}}{D}$	Convective to diffusive mass-transfer ratio
Re	$\frac{\Delta\rho_l v_{sg} d_o}{\mu}$	Inertial to viscous forces ratio
Ar*	$\frac{\Delta\rho^2 d_o^3 g}{\mu^2 \varepsilon}$	Buoyant to viscous forces ratio
Sc	$\frac{\mu}{\rho_l D}$	Hydrodynamic to concentration boundary layer thickness ratio

The definitions of the dimensionless groups, along with their interpretations are shown in Table 5.

CHAPTER 4

EXPERIMENTAL

4.1 Experimental Design and Description

This chapter describes the diffusion cells used to simulate the transport behavior in the DBCSR. The individual components and methods used to construct the cell, the analytical method, and experimental background are discussed.

Diffusion Cell Components

Lab scale diffusion cells are fabricated to measure transport rates, with geometry similar to the DBCSR. The diffusion cell shown in Figure 10 is similar to that design that would be employed on an industrial level.

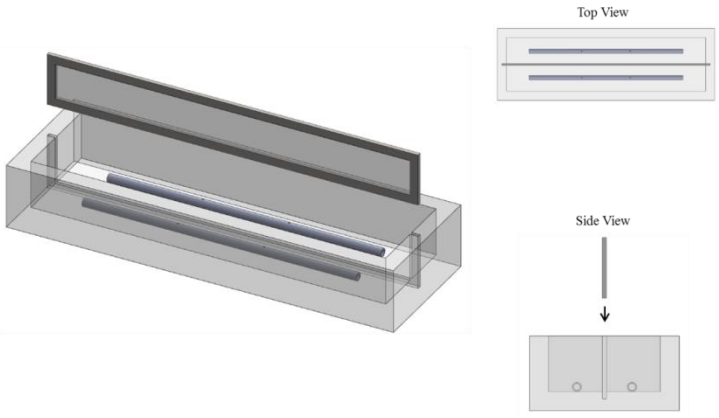

Figure 10. A schematic of the diffusion cell used to obtain the mass-transfer correlation.

The schematic shows walls and a base as the body. The walls and base of the cell are made from clear polycarbonate purchased from McMaster-Carr. The channel length,

perpendicular to the transport width occurring from channel to channel, is purposely sized much longer than the width. Gas sparging tubes are fixed in place on the base of the cell. The tubes are made out of clear, acrylic, and flow enters the tubing from both ends. A thin metal frame which holds a filter paper separator slides into grooves in both the walls and the base. The metal frame, similar to a picture frame, is fabricated from 316 stainless steel sheets purchased from McMaster-Carr. Filter paper, Grade 1, 11 μm pore size, is purchased from Whatman™ in sheets that are 58 cm by 68 cm in size. Two cells of different widths are made and are labeled 'Cell 1' and 'Cell 2.'

Table 6. The dimensions of the cells.

Name	Component	Value	Units
Cell 1	Length	56	cm
	Width	20	cm
	Height	10	cm
Cell 2	Length	56	cm
	Width	40	cm
	Height	10	cm
Whatman™ Filter Paper Separator	Length	55.9	cm
	Thickness	180	μm
	Height	9.3	cm
Acrylic Gas Sparging Tubes	Inner Diameter	12.7	mm
	Outer Diameter	19.1	mm
	Length	43.2	cm
	Number of Orifices (N_o)	$2 \geq N_o \geq 16$	--

A summary of the components and specifications of the cells are shown in Table 6. Both fabricated cell dimensions, along with the dimensions of the filter paper separator, and the dimensions of the gas sparging tubes are shown.

CO_2 Laser and Orifice Size

The orifices are cut into the acrylic gas sparging tubing using a CO_2 laser. The laser has much higher precision than using drill bits to make orifices. Additionally, the laser carves orifice

diameters much smaller than the smallest drill bits. The pressure drop across the orifice, from the inner tubing to the surrounding solution, increases as a result. The increased pressure drop along the length of the orifice effectively allows the system to be run at flow rates that are in line with those anticipated in an industrially sized reactor.

Two orifice diameters are used to determine the effect of orifice diameter on the mass-transfer rate. These orifice sizes are used in conjunction with a variable number of orifices.

Table 7. Gas sparging tube design.

Orifice Diameter (mm)	Number of Orifices (N_o)
0.26 ± 0.05	$2, 6, 10, 12, 16$
2.38 ± 0.10	$2, 6, 10, 12, 16$

Table 7 shows the combinations of orifice diameters and number of orifices used to determine the effect of orifice size on mass-transfer rate. The orifice diameters shown are the smallest and largest diameters that are used to form bubbles at the orifice. The 0.26 mm orifice diameter is a result of the smallest sized holes that are able to be made using the CO_2 laser. The 2.38 mm orifice diameter is made drilling a hole using micro-drill bits into soft plastic tubing. As shown in Figure 11, the soft plastic tubing is then wrapped around the sparging tubing, which already has 0.26 mm orifices.

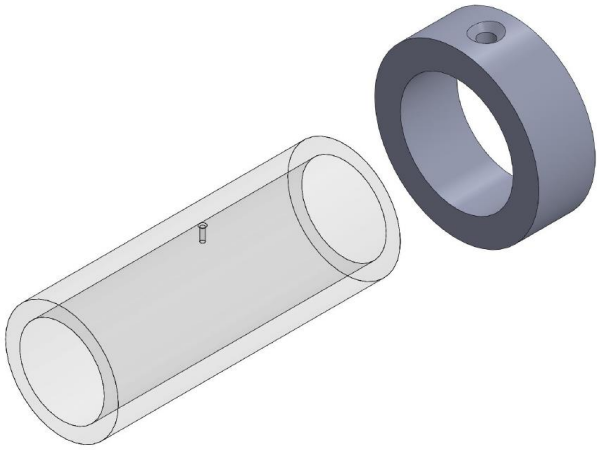

Figure 11. Soft plastic tubing is used to alter the orifice size on the gas sparging tubes.

The soft plastic tubing is wrapped around the orifice, ensuring a tight seal, and because of the cohesive forces of the surface tension of water, the 2.38 mm orifice diameter completely fills before a bubble is formed. Note that the bubble sizes are not the same as the orifice diameters.

The goal is to have bubbles forming at each orifice at a set inlet gas flow rate, with a minimum amount of gas flow required. Hence, the number of orifices is a function of the flow rate used. For example, when the inlet flow rate into the tube is low enough, such that bubbles do not form at each orifice, then the number of orifices is decreased until bubbles form from each orifice. In the case of flow rates near zero, the number of orifices at either orifice diameters is 2. As flow rates become larger than $1\ L \times min^{-1}$, the number of orifices used is 16. In between, 6, 10, or 12 orifices are used.

Flow Tubing, Rotameters, and Accessories

Soft plastic Masterkleer™ silicon tubing is purchased from McMaster-Carr™ to flow gas through the channels. The soft plastic tubing is selected with a smaller diameter than the

sparging tubing so that the gas sparging tubing is sealed at the ends where the soft plastic and hard acrylic tubing met. This arrangement prevents gas leaks in the line leading from the rotameter to the sparging tubes. Filtered building air is used as the sparging gas.

Rotameters were purchased from Omega™. Calibration curves are provided with the rotameters for various fluids, including air. The filtered air is plumbed directly to the inlet of the rotameters. Inlet gas is metered at the rotameter by noting the position of a weighted ball contained in the flow path of the rotameter casing. The ball responds to both the effects of gravity and inlet gas. As a result, the rotameters are oriented vertically. A wall is built from polycarbonate to hang the rotameters on, and their orientation is measured by a level to ensure that they are aligned vertically.

Needles and syringes are used to sample the channels of the cell. The needle syringe combination is purchased from BD syringes. Sparging tubes are held in place with nylon straps, one piece attached to the base, the other piece wrapped around the outside of the tubing.

Pressure drops are experimentally measured using a General Tools™ DM8230 Deluxe Digital Manometer.

4.2 Experimental Procedure

First, the channels of the cell are cleaned using type 1 deionized and distilled water to remove as many residual ions or impurities as possible. Then, the sparging tubes are put in place. The location of the spargers depends on the type of study. Generally, the sparging tubes are located in the center of the channel, along the length of the channel. The channels are then filled with deionized water up to a liquid level line that completely submerges the cross sectional

area available for transport through the filter paper separator. The liquid is allowed to sit for several minutes to allow any residual electrolyte to reach equilibrium in the cell. After ensuring that the separator is secure and sturdily in place, thin polycarbonate rectangular bars are placed adjacent to the separator frame. These bars help prevent any splashing over the frame that could influence the concentration in the channels.

At time equals zero minutes, the channel is sampled to determine the starting ion concentration in the cell. This concentration is subtracted from the each measured concentration along the length of the experiment, as it is residual ion left from the previous experiment. After zero time sampling, the rotameters are checked to ensure that the correct gas flow rate is being used for the experiment. After ensuring that the flow rates are set to the correct values, known masses of lithium chloride and potassium chloride are added separately to the channels. The contents of each channel are then stirred to ensure a uniform concentration cell from as early on as possible. The channels are referred to as either a donor or receiver channel. The lithium chloride donor channel is selected in the early stages of the experimental process to determine the mass-transfer coefficient. This means that the measurements in this work are based on the measureable concentrations of potassium chloride.

Potassium chloride leaves its donor channel, and the electrolyte enters the lithium chloride donor channel. Over time, the concentration is measured. As a side note, in order to prevent any mechanical gradients, any amount of fluid removed from a channel is simultaneously replaced with deionized water of the same volume. This procedure helps ensure that any sort of convection to through the filter paper is from random pressure changes and not

due to some sort of systematic error. The concentrations are measured using an ion chromatograph.

4.3 Choosing the Chemistry and Ion Chromatography

Lithium chloride and potassium chloride are chosen as the transporting species because their concentrations are easily measured by ion chromatography. A Thermo Scientific Dionex™ ICS-2100 Ion Chromatography System is used to measure the lithium and potassium chloride concentrations. The ICS-2100 has a real-time liquid eluent generation system, a sampling port, a pumping mechanism, a liquid guard and column combination, a suppressor cell to enhance the eluting species conductivity, a conductivity cell, and Chromeleon™ software that serves as a data collection point. Typically a calibration curve is made prior to running any samples. After running a sample, the type of species and its concentration are identified based on the standards set by the calibration curve. For a sample, a plot showing the peak area versus time is produced, which is referred to as a chromatogram of the sample. From the chromatogram, Chromeleon™ software calculates the concentration of the peak. Figure 12 shows the flow path for the injected solution.

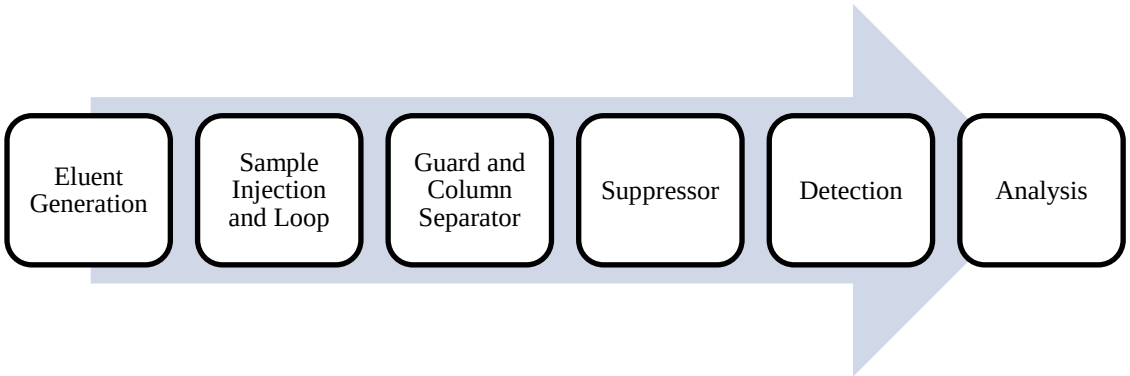

Figure 12. The ICS-2100 flow path.

A summary of the plumbing of the chromatography system is as follows:

1) A solution, referred to as eluent, is generated from an eluent generator cartridge and deionized liquid water. The eluent is then pumped into an injection valve.
2) At the injection valve, the sample is mixed with the pressurized eluent, and enters a degassing unit to remove the majority of the gas from the sample. After leaving the degassing unit, the sample enters a guard, at which point hazardous species are removed from the sample. After exiting the guard, the sample enters a separations process.
3) In the separating column, the ionic species in the sample are separated, based on their affinity towards the polymeric resin that lines the walls of the column. As a result of the separating process, chemically different ions exit the column at separate times.
4) The solution carrying the ions then enters a suppressor cell, which enhances the conductivity of the sample ions while, at the same time, suppressing the eluent conductivity.
5) The ions are detected a conductivity cell, which takes an electrical conductivity reading and converts the conductance into a peak. The culmination of all of the peaks in the sample is used to create a plot of peak area versus retention time. The peak areas are then converted to measureable concentrations based on the calibration curve.

The concentration of the eluent is set prior to injecting a sample. Setting the eluent concentration ensures that, for a specific concentration, individual peaks for the sample ions will consistently appear at or near an expected retention time. In this work, the concentration of the eluent, methane sulfonic acid, is set to 20 millimolar.

4.4 Experimental Data Sample

After measuring several concentrations over a time interval, each of the concentrations is non-dimensionalized by the equilibrium concentration. Then, the dimensionless concentrations are plotted as a function of sampling time. Data sampled from the diffusion cell are shown in Figure 13 for potassium chloride. Mass-transfer coefficients are fitted to the data.

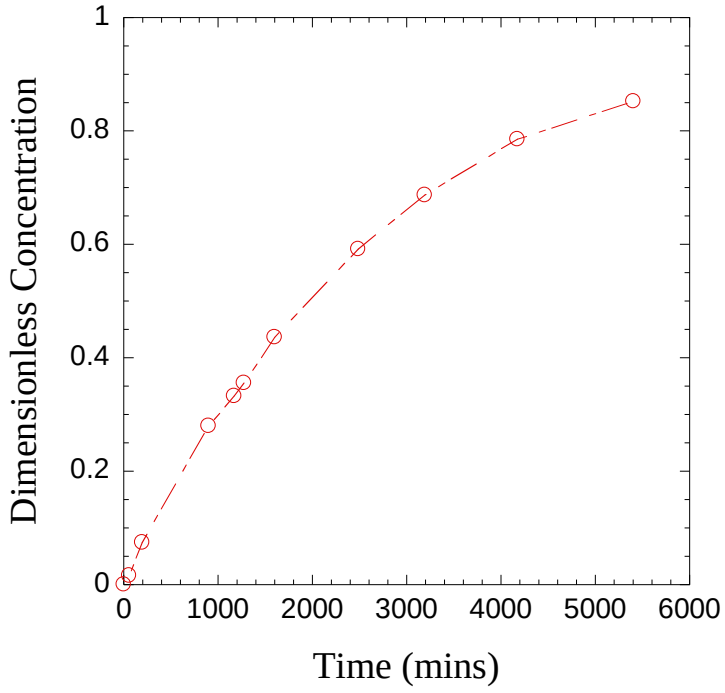

Figure 13. A plot of dimensionless concentration versus time in minutes for the lab scale reactor. Each dot represents a sampled point with a measured concentration.

The dimensionless concentration approaching a value of 1 physically represents the equilibrium concentration in the channel. That concentration is half of the starting concentration. Using a material balance, coupled with an equation describing the flux of ion as proportional to

the bulk concentration difference, where the proportionality constant is the overall mass-transfer coefficient, the equation used to fit the data is determined to be

$$c_2(t) = \frac{c_{1,i}}{2}(1 - \exp(\frac{-2K_{ov}A_c}{V_2}t)) \quad (1)$$

where $c_{1,i}$ is the starting concentration of the species, all initially in one channel, K_{ov} is the overall mass-transfer coefficient in the channel, A_c is cross sectional area of the filter paper that is available for transport, t is the time at which a concentration in the receiving channel is measured, V_2 is the volume of the fluid in the channel, and c_2 is the concentration in the receiving channel which is a function of time. As $t \to \infty$, the exponential term approaches zero, and the equilibrium concentration is approached. The derivation of this equation is presented in Appendix C.

The exponential rise equation fitting tool found in Kaleidagraph™ is used to determine the mass-transfer coefficient from the plotted data. R^2 values are typically greater than 0.99. Two corrections are accounted for in the calculations to determine the mass-transfer coefficient. These two corrections are for evaporation and splashing.

4.5 Corrections for Evaporation and Splashing

Volume changes over the cycle of each experiment are accounted for. Splashing losses, resulting from channel solution unintentionally leaving the channels due to bubble rise, and evaporation losses are the two effects that are addressed. Splashing of the material is negligible, because the bulk of the solution is assumed to be well mixed. Hence, the channels have the same concentration of material throughout and so if splashing does occur, then the overall solution

concentration does not change because any material lost has the same concentration as the channel solution. Evaporation is taken account by two separate phenomena. The first phenomenon is from evaporation that is the result of the cell being exposed to a surrounding air environment. This rate is experimentally determined by measuring height differences in both chambers over time. For example, the total evaporation rate over the entire smaller cell is determined to be approximately $187\ \mu L \times min^{-1}$. The evaporation rates for both cells per channel are listed in Table 8.

Table 8. Evaporation rates for the cells.

Name	Channel Width (cm)	Evaporation Rate Per Channel $\mu L \times min^{-1}$
Cell 1	10	93.5
Cell 2	20	187

The total amount of water lost from evaporation is then computed to be

$$V_{evap} = \dot{V}t \tag{2}$$

where $\dot{V}$ is the volumetric flow rate of air into the channel, t is the time that the experiment is run, and V_{evap} is the total volume of water lost to evaporation.

As for the second phenomena, because of the sparging effect, the unsaturated, compressed air plumbed from the rotameters into the channels becomes saturated with air. The air is assumed to be completely saturated on leaving the channels. This effect can be significant at higher flow rates of gas which justifies a correction to the entire system volume. Table 9

shows the room characteristics used to compute liquid losses by flowing unsaturated air through the channels.

Table 9. Determining losses by saturation.

Room Characteristics	Value
Temperature	21° C
Pressure	101.325 kPa
P_{vap} (H_2O)	2.337 kPa

By taking the ratio of the vapor pressure of water to that of the total room pressure, the fraction of water in air is calculated. This value, multiplied by the dry air flow rate, is then the total amount of water lost from the channel to the bubbling gas. That is,

$$V_{out,bubble} = \frac{P_{vap}\dot{V}}{P}t, \tag{3}$$

where $\dot{V}$ is the volumetric flow rate of air into the channel, P_{vap} is the saturated vapor pressure of water in air, P is the total pressure, t is the time that the experiment is run, and $V_{out,bubble}$ is the total volume of water lost as a result of bubbling. The total volume of water lost to both evaporation and bubbling is then

$$V_{tot,lost} = V_{evap} + V_{out,bubble}. \tag{4}$$

$V_{tot,lost}$, which is a function of time, is subtracted from the initial volume of the cell at each sampling time. The adjusted volume at each sampling time is then used to correct the measured concentration at each sampled point.

4.6 Bubble Velocity and Measuring the Void Fraction

Generally, bubble rise velocity is a function of the size of the bubble. As the size of the bubble increases, the bubble experiences a greater buoyant force, which results in a greater rise velocity [41]. Additionally, the holdup time, or the void fraction, is a function of the rise velocity in gas sparged systems. In any effort to increase mixing due to turbulence, bubble size is a critical independent variable to a system.

Void fraction, ratio of the total gas volume to the total volume in each chamber, is accounted for by both the sparging effect, $\varepsilon_{\text{sparge}}$, and the void volume resulting from the tubing that displaces solution in the system, ε_{tube}. That is,

$$\varepsilon_{tot} = \varepsilon_{\text{sparge}} + \varepsilon_{tube} . \tag{5}$$

$\varepsilon_{\text{sparge}}$ is determined by measuring the volume of bubbles at different orifice diameters and the residence time of those particular bubbles. That is,

$$\varepsilon = \varepsilon_{\text{sparge}} = \frac{v_{sg}}{v_{bubble}} \tag{6}$$

where v_{sg} is the superficial gas velocity of the gas bubbles and v_{bubble} is the bubble rise velocity which is experimentally determined. The superficial gas velocity, v_{sg}, is given as

$$v_{sg} = \frac{\dot{V}_{air}}{A_{ch}} \tag{7}$$

where $\dot{V}_{air}$ is the volumetric flow rate of air into the channel and A_{ch} is the cross sectional-area of the channel. This cross sectional-area is computed as the product of the channel width and channel length. Figure 14 shows the length scales used to determine the cross-sectional area of the channel.

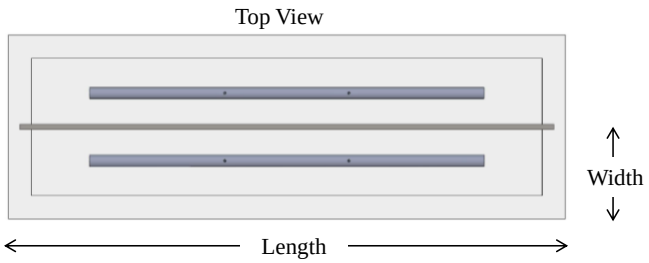

Figure 14. An illustration of the length scales used to determine A_{ch}.

A video camera is used to capture a recording of the bubble rising in a chamber, and the dimensions of the bubble are measured. In general, because of the shallow liquid level, the bubble did not appear to deform significantly from a spherical shape. Hence, a spherical assumption is used to determine the average volume of bubbles at certain orifice sizes. Table 10 shows the bubble sizes and velocities for two different orifice sizes determined using the frame rate method discussed previously.

Table 10. Bubble rise velocities as a function of orifice size.

Orifice Diameter (mm)	Bubble Size (mm)	v_{bubble} ($m \times s^{-1}$)
0.26	3.5	0.11
2.38	5	0.16

Note that the as superficial gas velocity increases, the bubbles leaving the orifice as subjected to increasing forces, and shearing of single bubbles into smaller bubbles occurs at the orifice. Because of the breakup effect at high bubble rise velocities, the swarm of bubbles leaving an orifice is assumed to be the volume of a single sphere leaving the orifice, even at high gas velocities. This assumption is required because of the difficulties in determining individual bubble volumes for a swarm of bubbles. The total number of frames is used to determine the rate at which a bubble rises, where the rate is proportional to the residence time of the bubble. The time the bubble enters and exits the chambers is found by converting the frame rate from the number of frames per second, 30, to elapsed time. Both the total residence time and the volume calculations are used in determining the void volume.

Because ε_{tube} is found to be negligible relative to the volume of the channel, the total void fraction is expressed as

$$\varepsilon_{tot} = \varepsilon = \frac{v_{sg}}{v_{bubble}} \tag{8}$$

4.7 Experimental Data Points

The set of experiments are shown in two tables. The purpose of two sets of experiments is to independently determine the mass-transfer correlation with no variation on the positioning of the gas sparging tube, while also being able to independently determine the effect of varying the positioning of the gas sparging tube.

Table 11. Experiment set one: The Mass-Transfer Correlation.

Cell Number	Orifice Size (mm)	$\frac{\dot{V}_{air}}{\text{channel}}\left(\frac{\text{L}\times\text{min}^{-1}}{\text{channel}}\right)$
1	0.26	0.12, 0.31, 0.61, 1.22, 1.84
	2.38	0.12, 0.31, 0.61, 1.53
	--	0
2	0.26	0.07, 0.17, 0.52, 0.80, 1.22
	2.38	0.07, 0.17, 0.52, 0.80, 1.53
	--	0

The first set of experiments, shown in Table 11, is designed to determine the mass-transfer correlation for a sparger orientation in the center of the channel. The volumetric flow rate of sparged gas is shown per channel. The total volumetric flow rate through the cell is double the value shown in the table for each experiment.

Table 12. Experiment set two: Sparger Orientation.

Cell Number	Orifice Size (mm)	$\frac{\dot{V}_{air}}{\text{channel}}(\frac{\text{L}\times\text{min}^{-1}}{\text{channel}})$	Distance of Tube from Separator (mm)
1	0.26	0.12	18,50,65
	2.38	1.53	28,50,65
2	0.26	0.12	18,100,115
	2.38	1.53	30,100,115

The second set of experiments, shown in Table 12, is designed to determine the effect of the sparger orientation; i.e., proximity to the concentration boundary layer, on the mass-transfer coefficient. A cartoon that summarizes the changed parameters relative to the construction of the cell is shown in Figure 15.

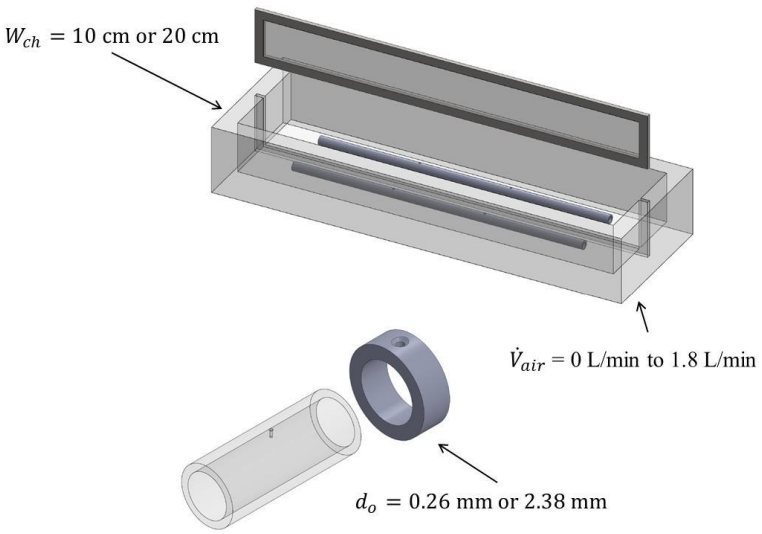

Figure 15. The parameters of the experiment in correspondence to the design of the cells.

The summary cartoon shows the channel width, volumetric flow rate of air, and orifice diameter parameters relative to the design of the cell.

Determining Error

Error bars are reported for the data shown. There are two sources of error addressed. The first source of error is the uncertainty in the inlet gas flow rate. The rotameters are accurate to $\pm 3\%$ of the gas flow rates. The error in the mass-transfer coefficient is expressed as a relative standard error. The relative standard error (RSE) is expressed as

$$RSE = \frac{\sigma}{\bar{\mu}}, \tag{9}$$

where σ is the standard deviation and $\bar{\mu}$ is the mean of the sample set. The *RSE* is determined to be 6.7 %.

Table 13. The relative standard error.

Number	$K_{ov}\left(\mathrm{m\times s^{-1}}\right)$	Flow Rate $(\mathrm{L\times min^{-1}})$	Orifice Diameter (mm)	$\sigma\left(\mathrm{m\times s^{-1}}\right)$	$\bar{\mu}\left(\mathrm{m\times s^{-1}}\right)$	*RSE* (%)
1	1.87×10^{-6}	0.61	0.26	1.20×10^{-7}	1.79×10^{-6}	6.7
2	1.70×10^{-6}					

The calculation is shown in Table 13. There are multiple repeated data points available to determine the relative standard deviation, which are not shown. However, these data have the highest relative standard error from the points available.

CHAPTER 5

Mass-Transfer and Energy Analysis

5.1 Overview of Results Sections

Before proceeding with a discussion of the analysis, a connection between the channel width and measuring mass-transfer coefficients must be made. Effectively, the wider the channel, the more mass transfer is needed to support the reaction. More mass transfer requires that there be a higher flux of the transporting species into the channel. As previously noted, the flux is directly proportional to the mass-transfer coefficient. Therefore, if a wider channel requires a higher flux, then in order to meet the demands of the reaction, the mass-transfer coefficient must increase. In turn, if gas sparging is to enhance mass transfer, then the mass-transfer coefficient must increase as a result of gas sparging the solution. Additionally, an increase in the mass-transfer coefficient is accompanied with a well-mixed bulk phase. Therefore, the low reactor utilization concerns, accounted for in Chapter 2, are addressed with increases in the mass-transfer coefficient.

Because the total gas flow rate is the most central input parameter, much of the results obtained center around its effects on the rate of mass transfer. The mass transfer is studied by the experiments outlined in Table 12 and Table 13. In the first set of experiments, the effect of the total gas flow rate on the Sherwood number for the combinations of cells and orifice diameters is discussed. Then, a channel mass-transfer correlation for both cells is given for the combinations of cells and orifice diameters. Following this discussion, the mass-transfer correlations that best represent the diffusion cells are presented. From the correlations, a range

of channel widths are discussed based on I^-, I_3^-. Then, in the second set of experiments, the effect of the orientation or position of the sparger in the channel is discussed for both cells. Finally, a discussion of the energy requirements closes this chapter.

The Sherwood correlations are proposed on the basis of values calculated for dimensionless groups at each experiment.

Table 14. Range of calculated values for the dimensionless groups.

Dimensionless Group	Range
Sh	$40 < \mathrm{Sh} < 560$
Re	0 (Stagnant Fluid) $0.01 < \mathrm{Re} < 1.2$ (Sparged Fluid)
Ar^*	0 (Stagnant Fluid) $1\times10^{4} < \mathrm{Ar}^* < 3\times10^{9}$ (Sparged Fluid)
Sc	453.2
$\frac{d_o}{w_{ch}}$	0 (Stagnant Fluid) $1\times10^{-3} < \frac{d_o}{w_{ch}} < 3\times10^{-2}$ (Sparged Fluid)
ε	0 (Stagnant Fluid) $9\times10^{-5} < \varepsilon < 1\times10^{-3}$ (Sparged Fluid)

A range of the typical values of each dimensionless group are shown in Table 14. Separate values are listed for stagnant fluids, sparged fluids, and either stagnant or sparged fluids.

5.2 Experiment Set One: The Mass-Transfer Correlation

Comparison of the Measured Sherwood Numbers for Both Cells

The purpose of experiment set one is to obtain a mass-transfer correlation that best describes the diffusion cells, without considering the sparger orientation. However, as shown later in the text, the cells are best represented by two correlations, primarily because the convection flow patterns in the cells are not similar. The measured species in all experiments is potassium chloride. The liquid diffusivity of potassium chloride is assumed to be $1.99\times10^{-9}\ m^2\times s^{-1}$ [32]. The mass-transfer coefficient for each experiment is determined by fitting experimental data, as mentioned previously. The Sherwood number, which is proportional to the mass-transfer coefficient, for cell 1 is plotted versus the channel gas sparging volumetric flow rate. The results for cell 1 are shown in Figure 16.

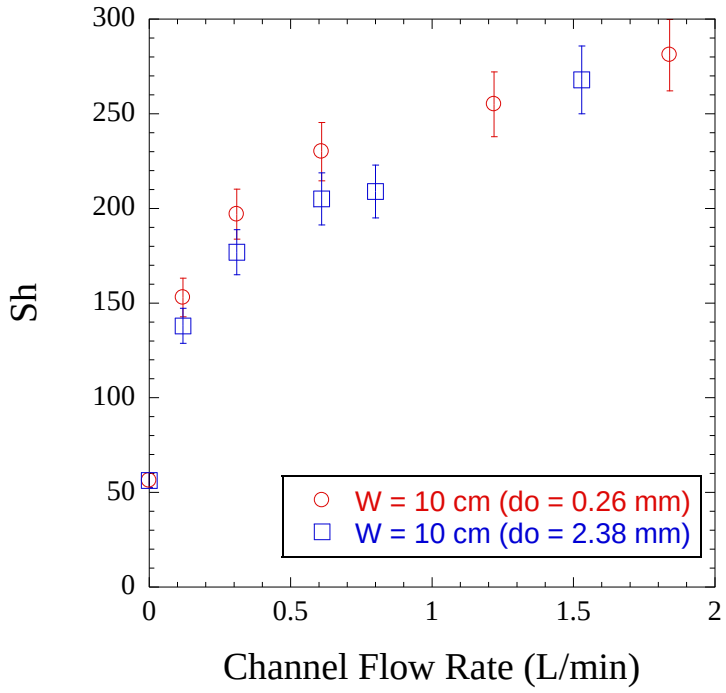

Figure 16. The Sherwood number is plotted as a function of the channel gas volumetric flow rate, which is an independent parameter. Cell 1 channels are 10 cm in width.

The figure shows the impact of the input air flow rate on the mass-transfer coefficient. The results indicate an intuitive observation: the Sherwood number increases by increasing the volumetric flow rate of inlet gas. This means, as discussed at the beginning of the chapter, that gas sparging enhances mass transfer. However, surprisingly enough, the orifice diameter has no significant impact on the Sherwood number. This is counterintuitive, as the larger orifice diameter intuitively creates larger bubbles. This result has been experimentally documented in Table 10. As the bubble size increases, larger bubbles experience a greater buoyant force, and in turn, a larger rise velocity. Because of this larger velocity, they generate an increased amount of turbulence in the system, typically resulting with better overall mixing [41, 45, 46]. However, this same trend is not observed here.

At zero gas flow rate, low rates of mass transfer are shown. In the initial channel gas flow rate rise, a high sloping Sherwood number is shown. This implies that not much gas is required to induce mixing in the system, thus enhancing the mass transfer. As the volumetric flow rate of the gas increases, the mixing effect tends to lessen, and eventually, the Sherwood number is expected to reach an upper limit despite an increase in gas flow rate. This maximum can be attributed to two possible effects. The first is a shearing effect, in which the bubble no longer leaves the orifice as a single large bubble but is sheared into smaller bubbles. The shearing effect lessens the bubble size, which in turn provides lessened mixing in the channel. The second is that, because the bubbles leave the orifice and rise directly upwards, the effects are only felt in and around a column above the orifice. Hence, any substantial rise in the sparging gas flow rate is only going to be felt near the fluid around the column, limiting mixing. If the liquid depth were not as low, then with the increasing bubble residence time, it is intuitive to expect a greater mass-transfer coefficient. With increasing liquid level, bubble to bubble interactions are likely to increase, and coalescence of bubbles is only expected to lead to better mixing [47]. However, because of the limitations imposed by the PEC cell requirements (10 cm channel depth), the system is tested at liquid depths of approximately 10 cm.

The same effect is seen in cell 2. Figure 17 shows the Sherwood number as a function of the channel gas flow rate.

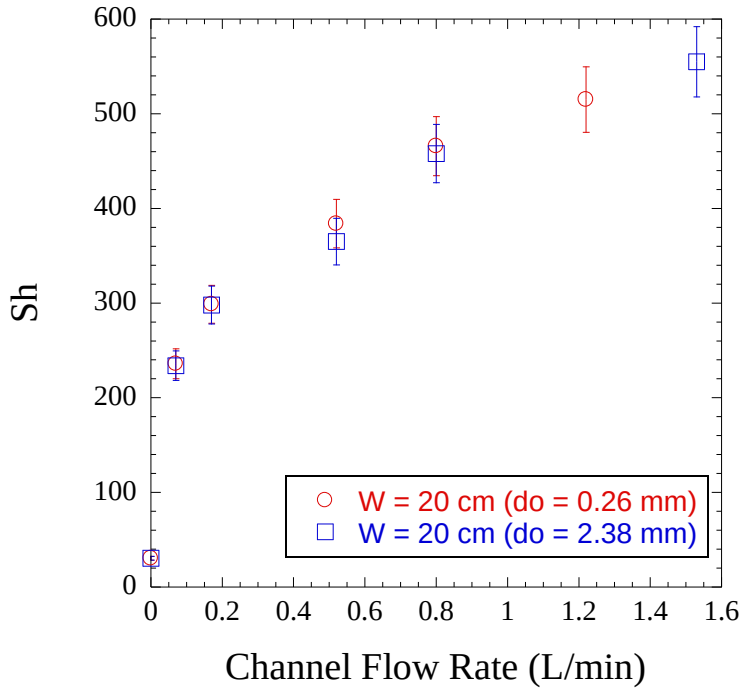

Figure 17. The Sherwood number is plotted as a function of the channel gas volumetric flow rate, which is an independent parameter. Cell 2 channels are 20 cm in width.

Comparing Figure 16 and Figure 17, at zero gas flow rate, the experimental results suggest that some transport is occurring in what is intended to be a stagnant fluid. However, at zero gas flow rate, it appears that the Sherwood number decreases as the cell size increases. Because of how the Sherwood number is defined, this means that the mass-transfer coefficient decreases with increasing cell size. This suggests that, as intuitively expected, as the channel width grows infinitely larger, the mass transfer rate is going to approach zero for zero gas flow rate. Also as in the smaller cell, the larger channels experience the same high slope at initial flow rates. Again, the effect tends to taper off and is expected to eventually reach an upper limit.

It is important to address the idea of a stagnant fluid in both cells, which is assumed the case at zero inlet channel gas flow into the channels. In the lab level experiments, the fluid feels

the effects of many small vibrations. For example, what might seem to be a trivial effect, a door closing, generates enough vibrations to induce some level of mixing in the fluid. This inability to control the level of stagnancy of the fluid would have been a major issue, had it not been for the fact that these reactors are located outdoors. Intuitively, the fluid in the reactors is likely to experience thermal gradients from the effect of the sunlight and the surrounding pavement and heats of reaction. These gradients are going to induce density differences in the fluid, causing natural fluid convection in the system. Hence, the vibration effect is likely relatively little compared to the actual thermal gradient induced mixing that the actual reactor will experience.

The results are not as conclusive if one is to compare the Sherwood numbers for both cells. As seen in Figure 18, the calculated Sherwood numbers for both cells suggests that the mass transfer is higher for the 20 cm channel width cell as compared to the 10 cm channel width.

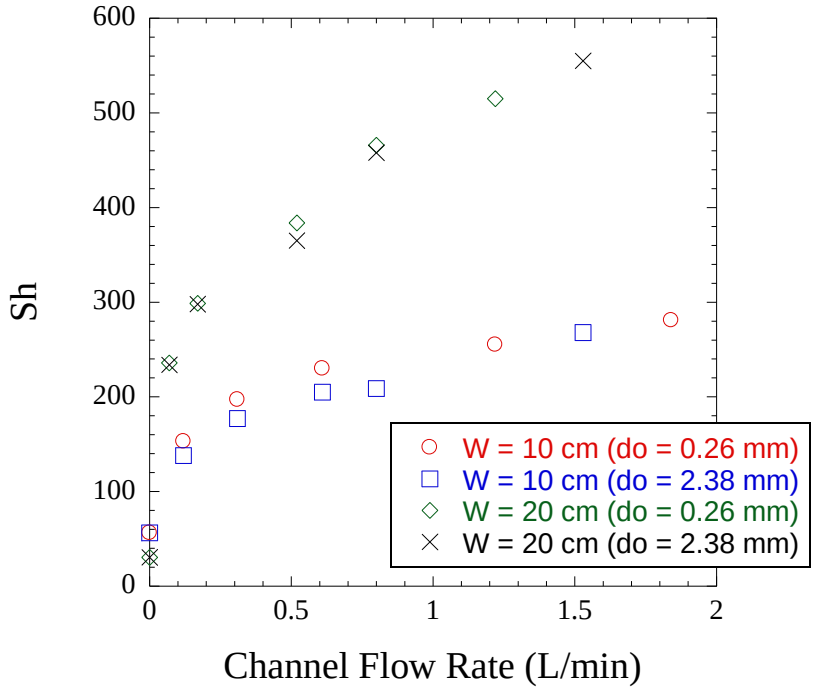

Figure 18. The Sherwood number is plotted versus the channel air flow rate for all combinations of orifice diameters and both cells. Error bars are not shown for clarity.

However, this is a consequence of how the Sherwood number is calculated. Because the Sherwood number is based on the channel width, the Sherwood number represents both the cell size and the mass-transfer coefficient. Because of this consequence of the definition of the Sherwood number, the channel mass-transfer coefficient, for potassium chloride, presents a better alternative in discussing the system mass transfer.

5.3 Experiment Set One: Revised for Channel Mass-Transfer Coefficient

The effect of varying the channel width on the channel mass-transfer coefficient is also examined for both orifice diameters. In Figure 19, the channel mass-transfer coefficient for potassium chloride is plotted as a function of the total flow rate in the cell for an orifice diameter of 0.26 mm. The mass-transfer coefficient appears to be nearly the same, with respect to the error in the experiment, for both channel widths.

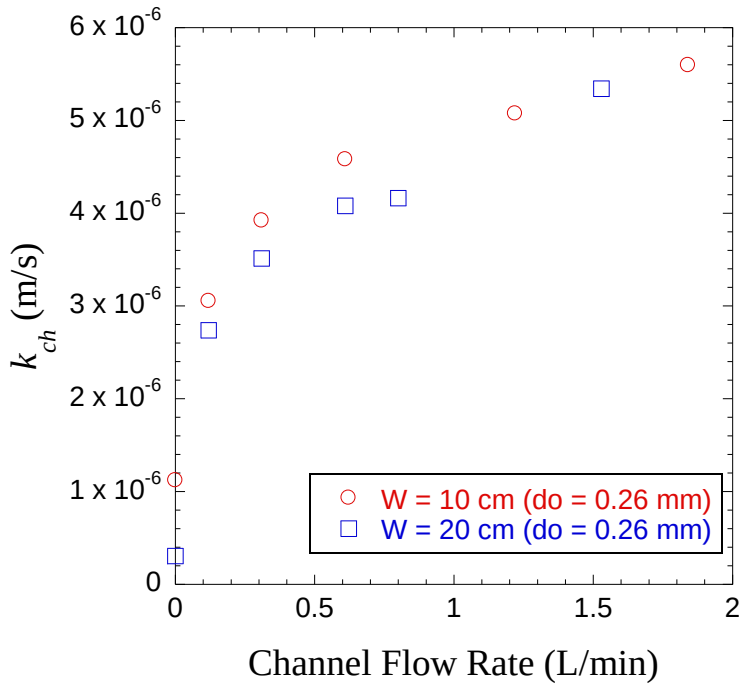

Figure 19. The channel mass-transfer coefficient for potassium chloride is plotted against the total system volumetric flow rate for an orifice diameter of 0.26 mm. Error bars are not shown for clarity.

The same type of analysis is done in Figure 20, in which the channel-mass-transfer coefficient for potassium chloride is plotted as a function of the total flow rate in the cell for an orifice diameter of 2.38 mm. Again, the differences in the transport coefficient are insignificant with respect to the channel width. This behavior is not as clear as in the case of using the Sherwood number to interpret the same results, as seen in the previous section.

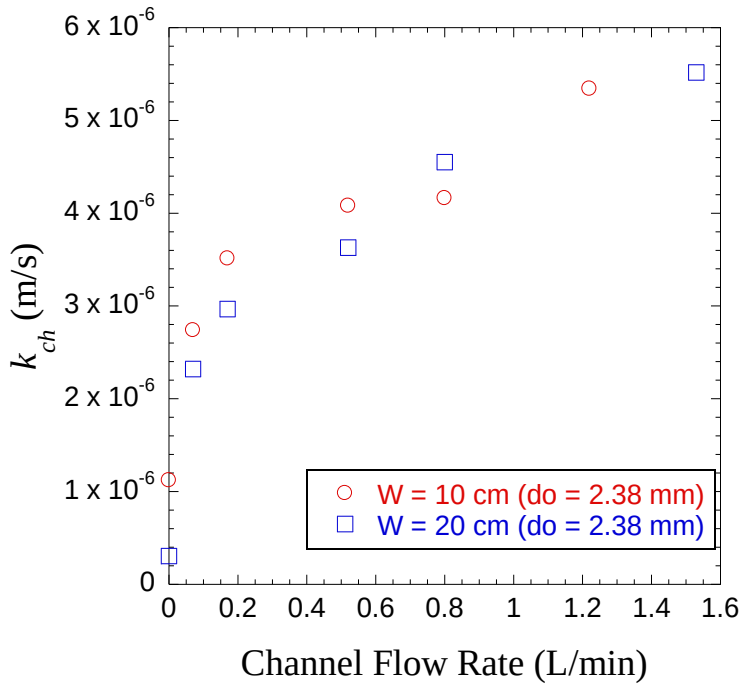

Figure 20. The channel mass-transfer coefficient for potassium chloride is plotted against the total system volumetric flow rate for an orifice diameter of 2.38 mm. Error bars are not shown for clarity.

Comparing Figure 19 and Figure 20, the transport coefficient appears to be independent of the orifice diameter. Also, despite containing twice the volume of solution, the transport coefficient appears to be the same for different channel widths in both figures. This result implies that the mass-transfer coefficient only weakly depends on the channel width. Therefore, a similar measured mass-transfer coefficient is to be expected with a larger or smaller reactor size, at least for the two widths studied here.

5.4 The Mass-Transfer Correlation for All Data

The mass-transfer correlation describing transport within a channel is determined by fitting the functional form of the correlation to the experimental data. The functional form is

$$\mathrm{Sh} = f\left(\mathrm{Re}, \mathrm{Ar}^{*}, \mathrm{Sc}, \frac{d_o}{w_{ch}}, \varepsilon\right). \tag{1}$$

The function is expressed in terms of six unknown parameters. That is,

$$\mathrm{Sh} = c_1 \left(\mathrm{Re}\right)^a \left(\mathrm{Ar}^{*}\right)^b \left(\mathrm{Sc}\right)^c \left(\frac{d_o}{w_{ch}}\right)^d \left(\varepsilon\right)^e \tag{2}$$

where, c_1, a, b, c, d, and e are all fitted parameters. At each experimentally determined mass-transfer coefficient, a Sherwood number is calculated. Along with the Sherwood number, the other five dimensionless groups are calculated because the experimental conditions are known. A non-linear regression is done on the data using Microsoft Excel™ to fit the data to the function. The final correlation for both cells is determined to be

$$\mathrm{Sh} = 0.009 \mathrm{Re}^{0.386} \mathrm{Ar}^{*0.250} \mathrm{Sc}^{0.333} \left(\frac{w_{ch}}{d_o}\right)^{1.182} \varepsilon^{0.116}. \tag{3}$$

A plot of the fitted versus experimental parameters is shown in Figure 21. The resulting fit has a sum squared error of 4.4%.

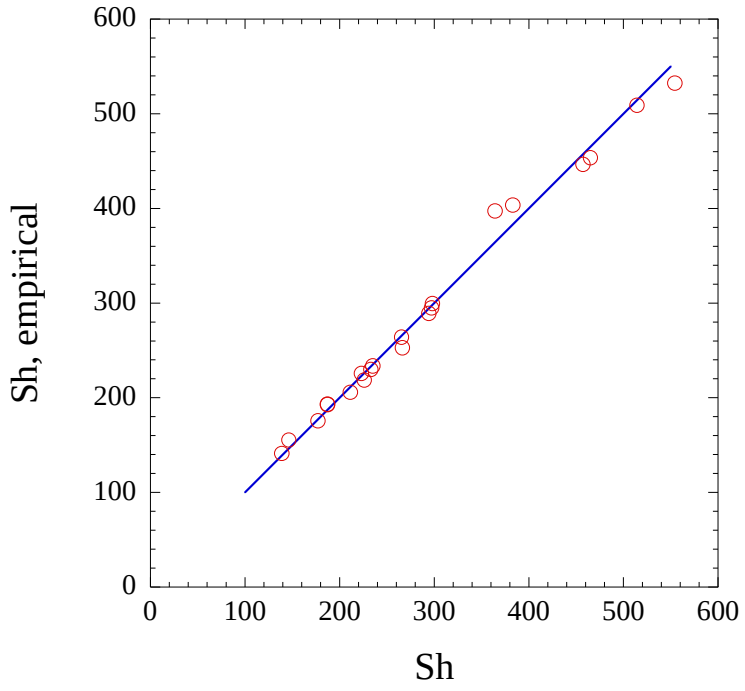

Figure 21. The fitting of the mass-transfer correlation to data for both cells.

The correlation tends to become less representative of the data at higher Sherwood numbers. This is a result of more experimental data available at lower values of the Sherwood number. Additionally, this correlation can be referred to as a working correlation.

5.5 The Mass-Transfer Correlations for Individual Cells

Mass-transfer correlations for the individual diffusion cells are an alternative way to present the experimental results. Because the results are only limited to two cell sizes, an overall correlation is not meant to be universal for all channel widths. Additionally, the diffusion cells have the same channel length and channel depth, but because of the differences in channel width, the convection patterns in each cell appear to be different. This is better justified section 5.6. The final form of the correlation for cell 1 is

$$\mathrm{Sh} = 0.039\mathrm{Re}^{0.272}\mathrm{Ar}^{*0.226}\,\mathrm{Sc}^{0.333}\left(\frac{w_{ch}}{d_o}\right)^{0.999}\varepsilon^{0.180} \tag{4}$$

A plot of the fitted versus the experimental parameters is shown in Figure 22. The resulting fit has a sum squared error of 1.04%.

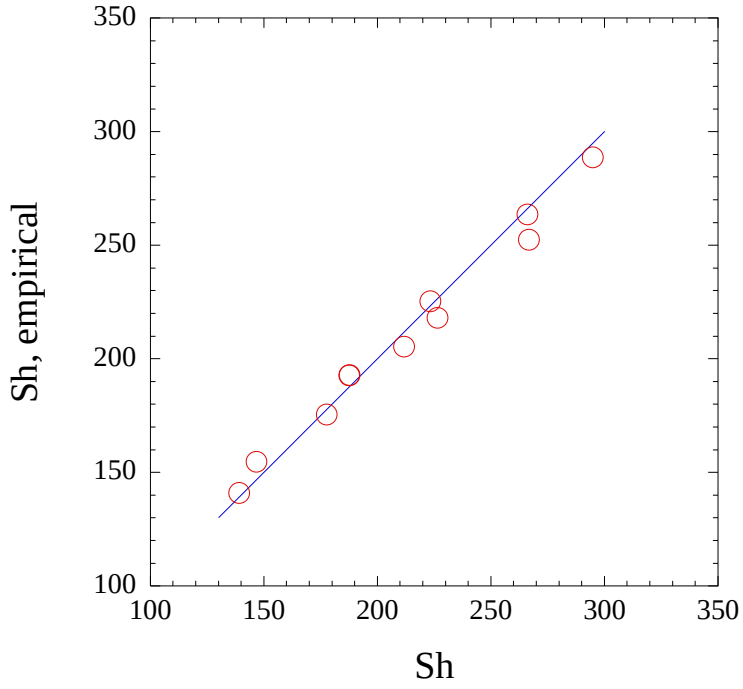

Figure 22. The results of the data fitting for cell 1.

The same type of correlation is determined for cell 2. The final form of the correlation for cell 2 is

$$\mathrm{Sh} = 0.030\mathrm{Re}^{0.423}\mathrm{Ar}^{*0.196}\,\mathrm{Sc}^{0.333}\left(\frac{w_{ch}}{d_o}\right)^{1.042}\varepsilon^{0.045} \tag{5}$$

A plot of the fitted versus the experimental parameters is shown in Figure 23. The resulting fit has a sum squared error of 1.43%.

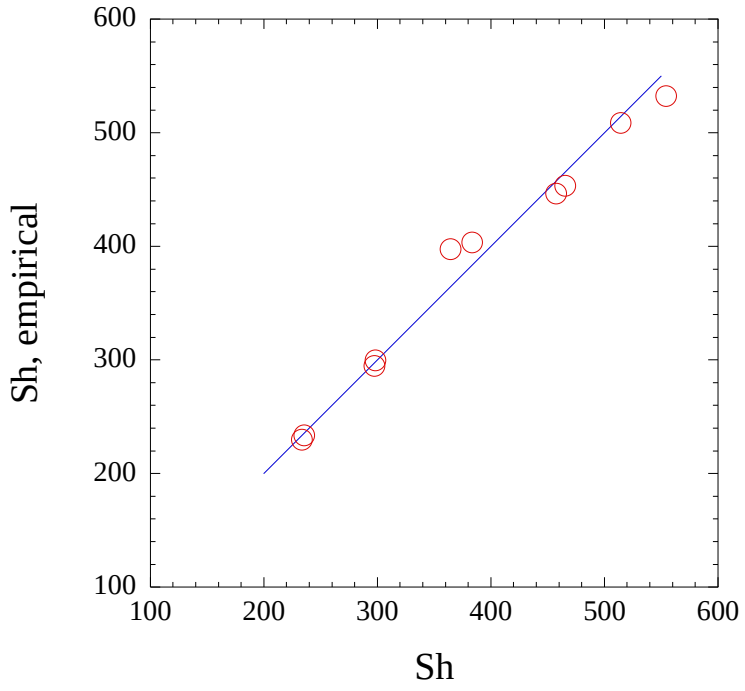

Figure 23. The results of the data fitting for cell 2.

All correlations show positive exponents for the Reynolds number. The fittings are sensible, as the Reynolds number is defined as a function of the superficial gas velocity. And, as the superficial gas velocity increases, the mass-transfer coefficient increases over the range of data shown. The correlations also show a positive exponent for the modified Archimedes number. Values for the exponent for the modified Archimedes number in the literature are typically around 0.25 [41]. The exponent of the Schmidt number is set by the Blasius solution to laminar flow over a flat plate [32]. The exponent of the dimensionless length ratio suggests that the Sherwood number is approximately directly proportional to the channel width but inversely proportional to the orifice diameter. This is the result of the definition of the Sherwood number using the channel width as the length argument. Additionally, the experimental results support the idea that as the orifice diameter increases, the Sherwood number decreases. The exponent

for the void fraction is positive as well. This fitting is in line with the experimental results because both smaller bubbles and high gas flow rates give larger void fractions in the solution.

5.5 Experiment Set Two: The Sparging Orientation

In this set of experiments, the effect of the sparging tubes proximity to the filter paper is examined. Figure 24 shows the results for cell 1. The behavior at lower and higher channel gas flow rates, $0.12\,\mathrm{L\times min^{-1}}$ and $1.53\,\mathrm{L\times min^{-1}}$, respectively, is shown.

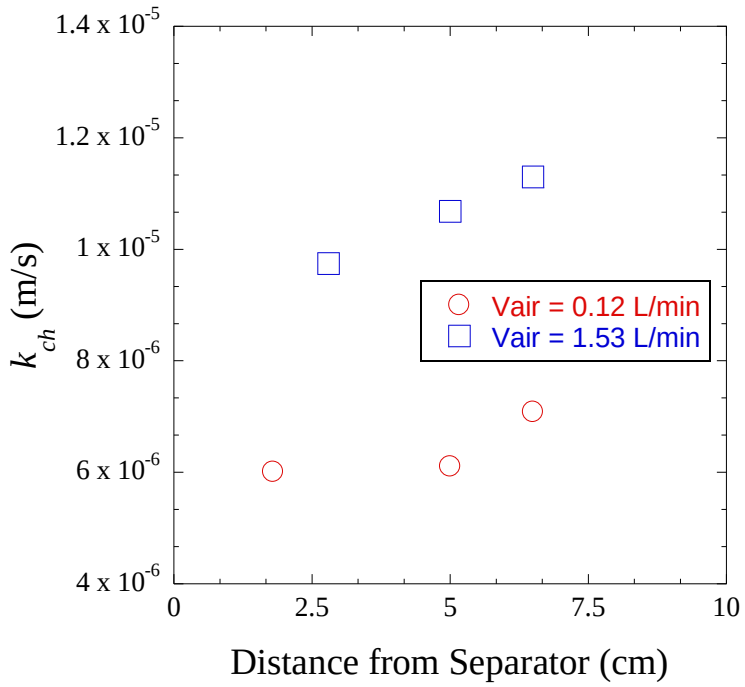

Figure 24. The effect of the sparger position on the channel mass-transfer coefficient for cell 1.

Each data point represents the position of the sparger relative to the separator. In both cases, the mass-transfer coefficient increases by moving the sparger further from the separator. This is not intuitive, as one would typically expect the concentration boundary layer thickness to be reduced by bringing the sparger closer to the separator.

The effect of the sparging tube proximity to the filter paper is also examined for cell 2. The results are shown in Figure 25.

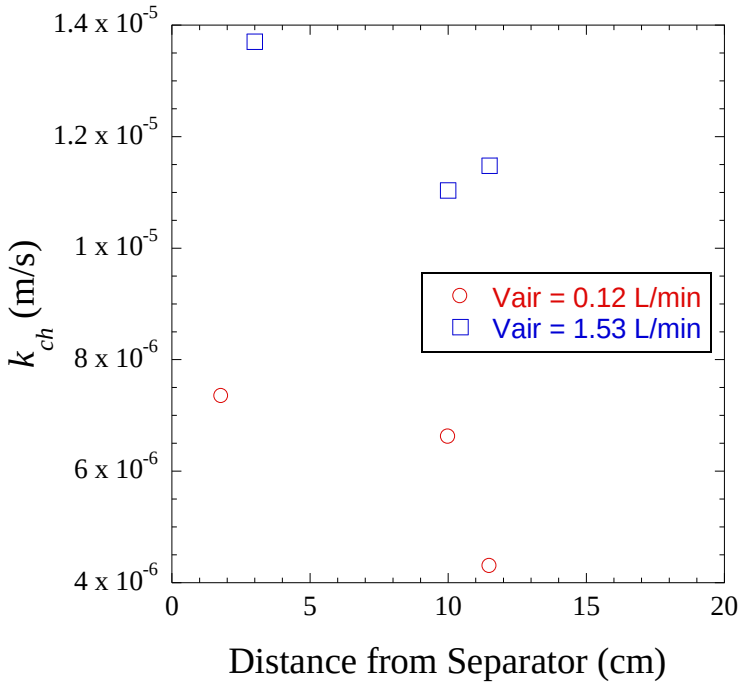

Figure 25. The effect of the sparger position on the channel mass-transfer coefficient for cell 2.

The slope of the line is trending down, which is opposite to what is seen in Figure 24. Hence, Figure 24 and Figure 25 support the idea that the convection that occurs in each cell is unique to that cell. Therefore, it is only reasonable to represent cells 1 and 2 with individual mass-transfer correlations. The results from the use of these correlations can be compared to better predict the behavior of different channel width cells.

5.6 Using the Correlations to Predict Energy Consumption

The purpose of this section is to predict the total energy consumption rate for sparging the solution to ensure the solution is well-mixed based on different potential reactor sizes.

Before proceeding, it is important to note that the correlations developed in this text are useful for any chemical species in order to predict energy consumption as a result of pumping gas into the channels. This text focuses on I^-, I_3^-. However, an energy consumption analysis can be done on any shuttling species as long as the diffusivity of the species is known. This text only provides an example of how to use the correlations to predict energy consumption rates. Additionally, this section assumes channel widths and from those widths calculates energy consumption rates. However, the opposite scenario is plausible. That is, a reactor width can be predicted by fixing an energy consumption rate.

Measuring Pressure Drop

In order to calculate the work required by gas sparging, the diffusion cell experimental pressure drop is experimentally measured using a General Tools™ DM8230 Deluxe Digital Manometer. This pressure drop is a measure of the pressure required to pump the gas through an orifice of approximately 0.26 mm into a head fluid of approximately 9.2 cm. A plot of the pressure drop as a function of the gas flow rate for two orifices is shown in Figure 26.

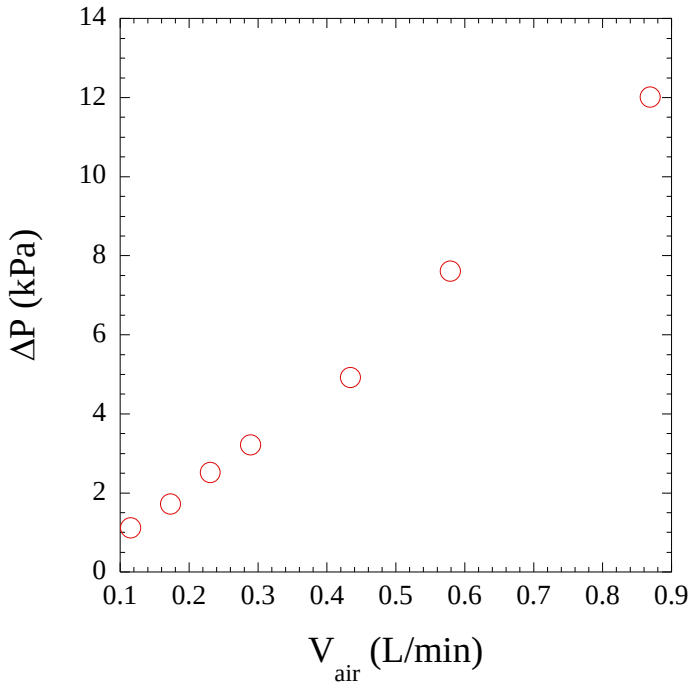

Figure 26. The experimentally measured pressure drop across the orifices of the sparging tube.

As the gas flow rate is increased, the pressure drop increases non-linearly. This is expected as the pressure drop is roughly proportional to square of the velocity, which is itself proportional to the volumetric flow rate. However, a pressure drop of 1.6 kPa, near the minimum gas flow rate shown in the plot, is chosen to best represent the pressure drops used in these experiments. This value is 150% of the minimal 1.1 kPa value and is used to be conservative. This value is chosen because at a slightly lower than this pressure difference (1.1 kPa from Figure 26), there is just enough gas flowing to have bubbles form at each orifice. In the experiments done in this work, the number of orifices is changed to ensure that there are just enough orifices in each experiment so that bubbling occurs at each orifice. Therefore, the pressure drop likely never exceeds this value of 1.6 kPa. If the pressure drop does exceed this value, the number of orifices is increased. Of importance to note is that, even though two orifice

sizes are used, the second orifice size is artificially generated as discussed previously. In result, the pressure drop for those sets of experiments is equivalent regardless of the orifice size.

Table 15. Parameters to determine sparging work.

Parameter	Value	Units
Δc	1	M
$D_{I_3^-}$	9.17×10^{-10}	$m^2\times s^{-1}$
ΔP	1.6	kPa
L_{ch}	0.58	m

The values for determining the work required are shown in Table 15. The diffusivity of I_3^- is $D = 9.17\times10^{-10}\ m^2\times s^{-1}$ and is used because its diffusivity is the smaller value of I^-, I_3^-, which limits the reactor size the most [48].

Scheme to Determine the Pump Work Required

Because solar irradiance is a function of the time of the day, the reaction rate changes throughout the day. This means that there exists the potential for large changes in the energy demands throughout the day. Figure 27 shows the scheme to calculate the parasitic losses resulting from gas sparging.

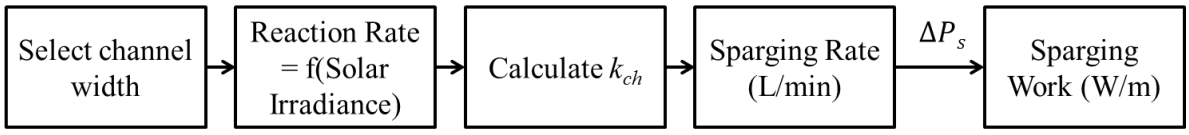

Figure 27. Scheme to calculate the pump work required for gas sparging the channels.

First, a channel width is selected. Then, the reaction rate is computed as a function of the solar irradiance. This value is then inputted into the material balance on each species, providing the channel mass-transfer coefficient for that particular channel width. The gas sparging flow is then computed, based on the correlations developed in this work. The work is then determined as the product of this gas flow rate and experimentally determined pressure drop. In the following text, the steps of the required work calculation are shown for one value of the solar irradiance, $10\,\mathrm{W}\times\mathrm{m}^{-2}$. Then, the calculation is repeated for several values of the solar irradiance, representing the work required at different times of the day.

Reaction Rate and Solar Irradiance

The reaction rate is dependent on the solar irradiance. As shown in Figure 28, the solar irradiance changes throughout the day [13]. Note that the plot is only an approximation of the solar irradiance and is only meant to be representative of the time dependent reaction rate.

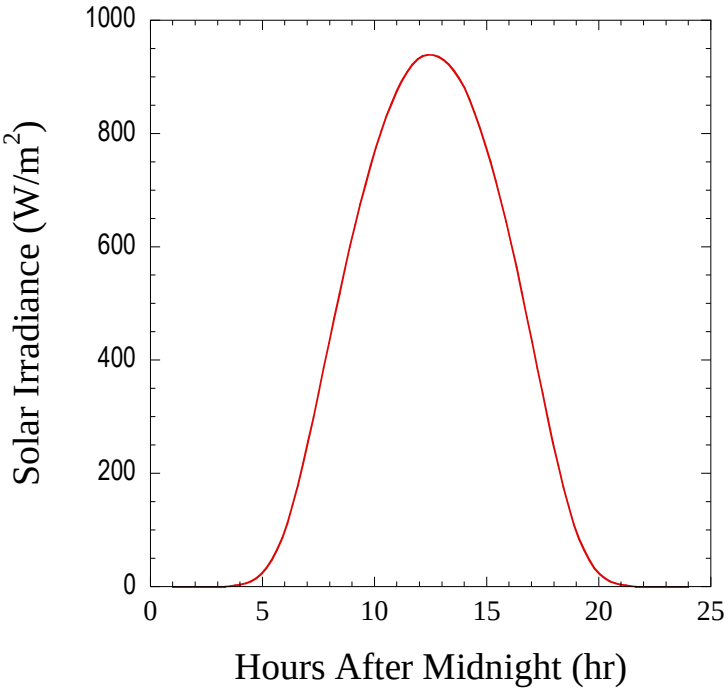

Figure 28. Solar irradiance versus the time of day. The values taken are for convenience.

Once the solar irradiance is known, the reaction rate needs to be determined. As stated in section 1.4, the reaction rate changes with the solar irradiance by

$$R_{H_2} = \frac{\eta_{STH} E_e}{LHV_{H_2} MW_{H_2} d_{ch}}. \tag{6}$$

Table **16** shows the reaction rate as a function of the solar irradiance for different times of the day. These values are used to calculate the required mass-transfer coefficient at that particular reaction rate.

Table 16. The reaction rate is shown as a function of the solar irradiance.

Solar Irradiance ($W \times m^{-2}$)	R_{H_2} ($mol \times m^{-3} \times s^{-1}$)
10	4.21×10^{-5}
200	8.42×10^{-4}
500	2.10×10^{-4}
1,000	4.21×10^{-3}

Calculating k_{ch}

The values for k_{ch} are determined using a steady-state material balance on a transporting reacting species in the reactor. That is,

$$K_{ov} \Delta c = R_{H_2} w_{cell} \tag{7}$$

where K_{ov} is the overall mass-transfer coefficient, ΔC is the concentration difference between the bulk phases, R_{H_2} is the reaction rate, and w_{cell} is the width of the cell. K_{ov} includes three resistances in series. Two are channel resistances resulting from the liquid solution, and the third is the membrane resistance. If the conditions are identical for both channels, then $k_{ch} = 2K_{ov}$ and $w_{cell} = 2w_{ch}$, with the resistance of the membrane being accounted for in the overall resistance, so that

$$\frac{k_{ch}\Delta c}{4} = R_{H_2} w_{ch} \tag{8}$$

where k_{ch} is the channel mass-transfer coefficient, and w_{ch} is the assumed channel width. This expression gives the relationship between the channel mass-transfer coefficient and the channel width. For example, for a given reaction rate and bulk phase concentration difference, a large reactor width requires a large mass-transfer coefficient. Therefore, for larger reactor widths, mass-transfer enhancements are required.

Sparging Rate (L×min^{-1})

Figure 29 shows the volumetric flow rate by sparging gas the solution. The values shown are based on variable channel widths but a constant reaction rate. A solar irradiance of $10\ \mathrm{W\times m^{-2}}$ corresponds to a reaction rate of $4.21\times10^{-5}\ \mathrm{mol\times m^{-3}\times s^{-1}}$.

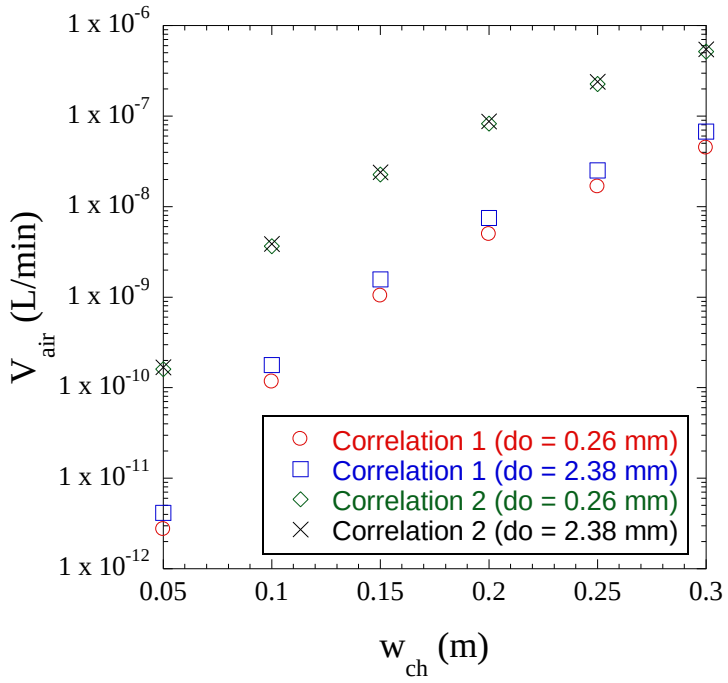

Figure 29. The volumetric flow rates required for gas sparging is shown. This is used to compute the work required to keep the channel solution well-mixed.

It is important to note that the results show the minimum amount of air needed to mix the solution. Sparging micro-liters of air into the reactor is unlikely. However, sparging any amount over this minimum value is likely to benefit the transport. Additionally, because the reactors are located outdoors, the natural convection in the channels may have the potential to satisfy the mass transfer demands, and therefore, no sparging would be necessary.

Sparging Work ($W \times m^{-1}$)

After determining the volumetric flow rates required to sparge the solution, the pressure drop is needed to determine the pump work. The pressure drop that is experimentally measured, which is listed in Table 15, is used. For convenience, the sparging work can be expressed in

terms of parasitic loss incurred as a result of using the product hydrogen as a fuel to power pumping equipment. The fractional loss is given as

$$Fractional\ Loss = \frac{H_2\ consumed}{H_2\ produced}. \tag{9}$$

The amount of hydrogen consumed is given as

$$H_2\ Consumed = \frac{(W/\Delta x)}{-\Delta G^o_{H_2} A_{ch}}, \tag{10}$$

where $W/\Delta x$ is the work per unit length, $\Delta G^o_{H_2}$ is the standard Gibbs free energy change from the combustion of H_2 and represents the maximum available work from the combustion of H_2, and A_{ch} is the cross-sectional area of the channel for which the depth is assumed to be 10 cm. $H_2\ produced$ is the reaction rate at which H_2 is generated in the channel, R_{H_2}. The combustion of hydrogen to form water is given as

$$2H_2 + O_2 \rightarrow 2H_2O. \tag{11}$$

The standard Gibbs free energy change for this reaction is given as

$$\Delta G^o = \Delta H^o - T\Delta S^o. \tag{12}$$

The standard Gibbs free energy change from the combustion of H_2 is given as

$$\Delta G^o_{H_2} = \frac{\Delta G^o}{n_{H_2}}, \tag{13}$$

where n_{H_2} is the stoichiometry of H_2 in expression (11). Table 17 shows the thermodynamic parameters used to determine the maximum available work upon combusting H_2.

Table 17. Thermodynamic calculation to determine work on combustion of H_2.

Parameter	Value	Units
ΔH^o	-483,619	$kJ \times kmol^{-1}$
ΔS^o	-88.73	$kJ \times kmol^{-1} \times K^{-1}$
ΔG^o	-457,179	$kJ \times kmol^{-1}$
n_{H_2}	2	kmol
$\Delta G^o_{H_2}$	-228,589.5	$kJ \times kmol^{-1}$

The thermodynamic parameters are taken from Engineering Equation Solver™ [49]. The fractional loss is then computed. Figure 30 shows the fractional loss incurred by sparging the solution through the channels for a solar irradiance of $10\ W \times m^{-2}$.

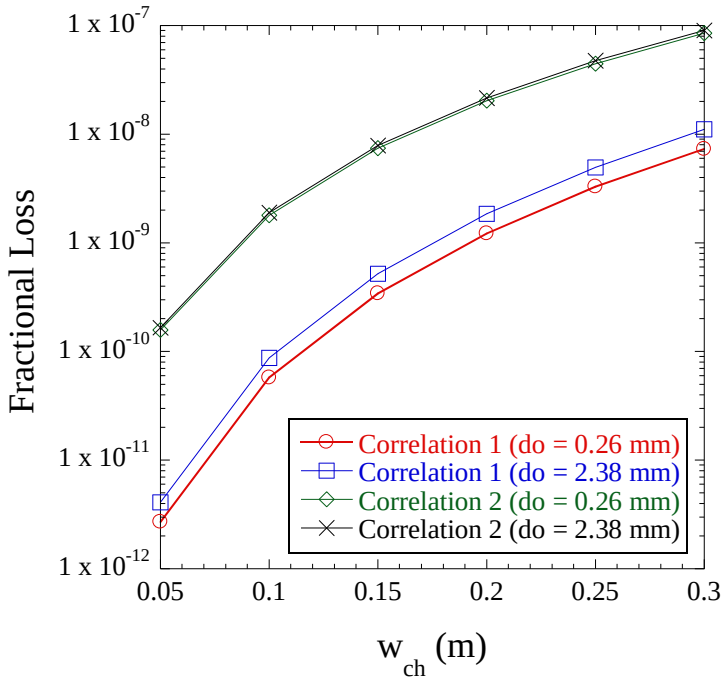

Figure 30. The fractional loss incurred by enhancing mass transfer is shown. The fractional loss is calculated for a solar irradiance of $10\,W\times m^{-2}$.

The fractional losses incurred by sparging the solution early in the morning or later in the afternoon range over four orders of magnitude depending on the channel width and over two orders of magnitude at each particular channel width. Hence, it is best to interpret the results more as a range of parasitic losses, rather than an absolute value. The same analysis is done for solar irradiances of 200, 500, and $1{,}000\,W\times m^{-2}$. Figure 31 shows the work required to sparge the solution through the channels for solar irradiances of 200, 500, and $1{,}000\,W\times m^{-2}$.

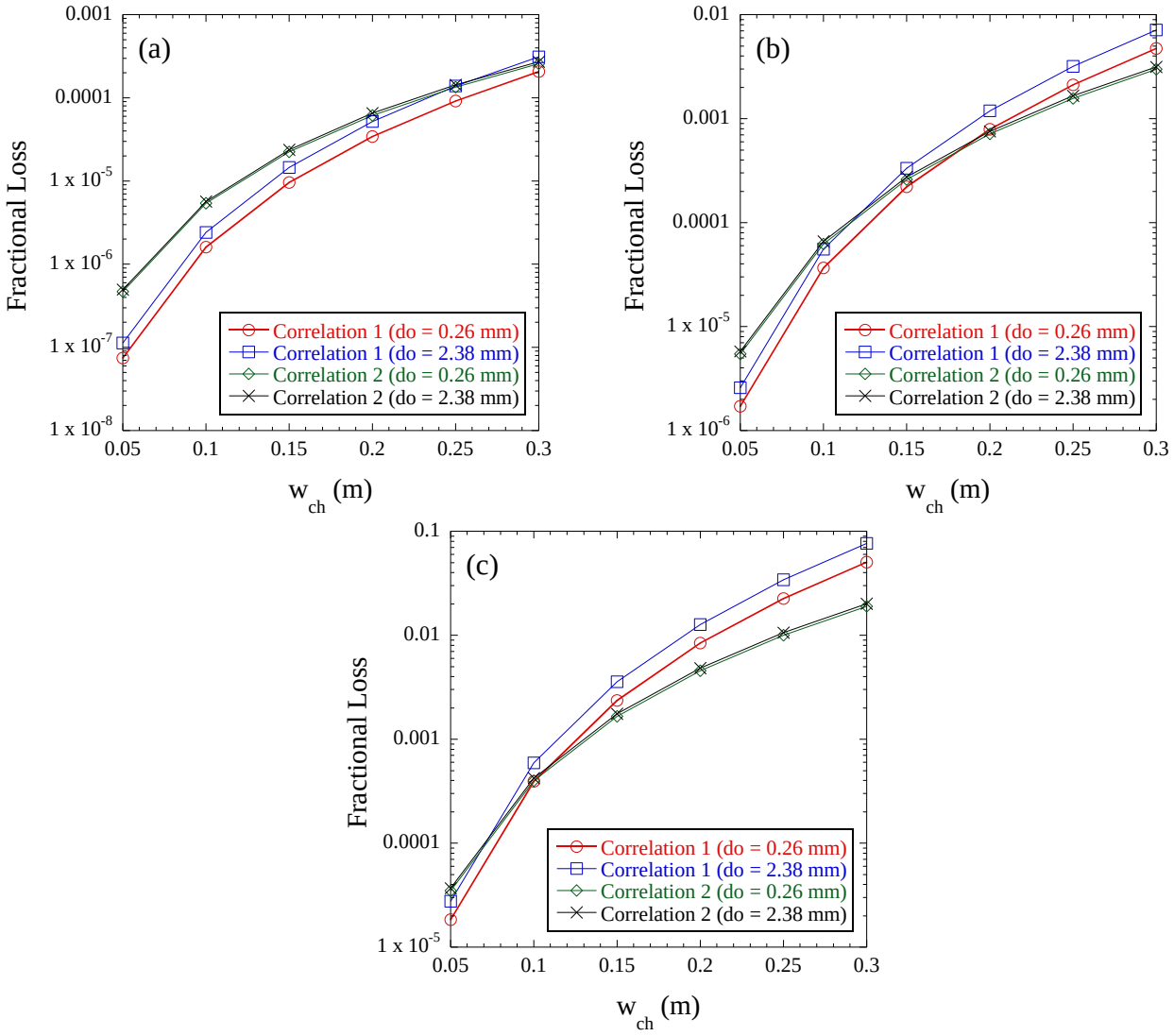

Figure 31. The fractional loss incurred by enhancing mass transfer is shown. The fractional losses are calculated for solar irradiances of (a) $200\,W\times m^{-2}$, (b) $500\,W\times m^{-2}$, and (c) $1{,}000\,W\times m^{-2}$.

For an increasing solar irradiance, parasitic losses as a result of sparging the solution increase. The parasitic losses from sparging the solution range from practically zero loss at $10\,W\times m^{-2}$, to almost ten percent at $1{,}000\,W\times m^{-2}$. This increase is attributed to an increased

demand of mass transfer at higher rates of reaction. That is, with an increase in the reaction rate, the required mass-transfer coefficient increases. Because the coefficient increases, the required gas flow rate used for sparging increases. In turn, this higher gas flow rate requires additional pumping power. However, it appears that even in the most drastic of cases, the parasitic losses that are predicted are still economical.

At lower values of the solar irradiance, it appears as if the correlations predict vastly different fractional losses. That is, the range of fractional loss for a particular channel width is over two orders of magnitude, and, it appears as if the first correlation is the better alternative. Then, the correlations begin to overlap, and eventually, the second correlation appears to be the best alternative. This behavior is a result of fitting the mass-transfer correlation expressions. If the parameters were fitted with different values, then one could reasonably expect different values. However, the same trends are expected to exist. That is, there is a range over which the fractional losses are to be expected. And, as the channel width increases, the fractional losses are expected to increase.

Of importance to note is that the correlations presented are themselves functions of channel widths. Because only two channel widths are used to determine the correlations, the correlations presented are not universal. This means that there is some inherent error likely in the required gas flow rates for different channel sizes. That implies that the values calculated for the work likely have some associated error as well. Therefore, it is better to use the correlations to provide a range of parasitic losses. Additionally, this work does not suggest that there exists some conclusive way to give a final width of the reactor. In initial designs, the reactor width spanned over an order of magnitude of 10 m. However, these lengths are unrealistic, as the

mass-transfer coefficient required is proportional to this width, given by expression (8). The mass-transfer coefficient of the redox mediating species required by this expression for reactor widths on the order of 10 m is much higher, on the order of 10^{-3} m×s^{-1}, than likely what is obtainable by sparging. More realistic widths are on the order of 10 cm, along the lines of what is used in this work.

5.7 Summary and Conclusions from Analysis

Because the channel width is proportional to the mass-transfer coefficient, any increases in reactor width must be accompanied with an increase in the mass-transfer coefficient. An increase in the mass-transfer coefficient requires an increase in gas sparging rates. This chapter develops mass-transfer correlations that are a function of the reactor width and gas sparging rates. Three correlations are shown for the diffusion cells fabricated to model the DBCSR and are used to estimate the mass-transfer enhancement requirements. The correlations are used to estimate the volumetric flow rate of gas needed to sparge the solution in the channels. The energy analysis shows that over a range of channel widths, gas sparging is an economical choice.

CHAPTER 6

CONCLUSIONS

6.1 Summary and Conclusions

The DBCSR is a conceptual reactor that is intended to be used with PEC cells to convert solar energy to chemical energy. A study is conducted on this reactor type. The results of the study provide several important conclusions:

1) Initial designs of the reactor are flawed. That is, mass-transfer rates are not considered. Modeling shows that the rates need to be enhanced.
2) Mixing the solution is a proposed method of mass-transfer enhancement. However, mixing the solution requires energy input, a form of a parasitic loss. The losses need to be mitigated. Gas sparging is proposed as a method to mix the reactor solution.
3) Experiments are devised to determine the energy usage. Mass-transfer correlations are established, and an energy analysis proves that gas sparging is an economical alternative, with respect to the solar irradiance.
4) The correlations that are established are limited, as the correlations are themselves a function of the reactor width, which is an unknown parameter.
5) The idea of different convection patterns in both diffusion cells is supported by experimental results, which describes the mass-transfer coefficient as a function of the sparger positioning.

The proposed mass-transfer correlations are useful in modeling various reactor widths. However, the mass-transfer correlations are not taken to be universal but can still be used to provide an estimate of potential channel widths and associated parasitic energy losses.

6.2 Future Work

These experiments are limited to only potassium chloride as the measured species. Experiments should be done to ensure that any other species is expected to have a similar Sherwood number for particular experimental conditions. Using more than one gas sparging tubes in each channel is also an area that needs to be studied. It is very likely that the same mass-transfer enhancement is expected, but the magnitude of the enhancement is unknown. Additionally, much larger cells than the ones used in this work could be built and tested. This would give a better idea of how the correlations developed in this work predict the mass transfer behavior in a larger cell. Finally, experiments with photocatalysts could be undertaken as well. These experiments would have a different set of goals, likely centering on the characterization of the photocatalyst.

APPENDIX A

1-D REACTION DIFFUSION MODEL DERIVATION

The Membrane Phase

In the membrane, no reaction occurs, as no colloidal particles are assumed to be present. The driving force for transport is the concentration gradient across the separator. The material balance and the net flux can be expressed by equations (1) and (2)

$$\frac{\partial c_A}{\partial t} = -\nabla \cdot N_A \tag{1}$$

$$N_A = -D_A \nabla c_A \tag{2}$$

Assuming a steady-state model with a constant diffusion coefficient through the separator phase.

$$0 = \frac{\partial^2 c_A}{\partial x^2} \tag{3}$$

The two boundary conditions can be expressed as at

$$x = -L \tag{4}$$

$$c = c_{A,1} \tag{5}$$

and at

$$x = L \tag{6}$$

$$c = c_{A,2} \tag{7}$$

Let the following non-dimensionalized parameters be expressed as

$$\overline{x} = \frac{x}{L} \tag{8}$$

$$\theta = \frac{c_A}{c_{A,i}} \tag{9}$$

And non-dimensionalizing the first boundary condition leads to

$$\overline{x} = -1 \tag{10}$$

$$\theta_{A,1} = \frac{c_{A,1}}{c_{A,i}} \tag{11}$$

And non-dimensionalizing the second boundary condition leads to

$$\overline{x} = 1 \tag{12}$$

$$\theta_{A,2} = \frac{c_{A,2}}{c_{A,i}} \tag{13}$$

Non-dimensionalizing the diffusion equation leads to

$$\frac{\partial^2 \theta}{\partial \overline{x}^2} = 0 \tag{14}$$

Integrating the non-dimensionalized reaction diffusion equation leads to the following expression

$$\theta = k_1 \bar{x} + k_2 \tag{15}$$

where k_1 and k_2 are integration constants.

The boundary conditions must be applied separately. Upon solving for the integration constants, the final separating phase integrated differential equation becomes

$$\theta = \frac{c_{A,2} - c_{A,1}}{c_{A,i}} \bar{x} + \frac{c_{A,2} + c_{A,1}}{2c_{A,i}} \tag{16}$$

$$\theta = \left(\theta_{A,2} - \theta_{A,1}\right) \bar{x} + \frac{\theta_{A,2} + \theta_{A,1}}{2}. \tag{17}$$

Equation (17) expresses the dimensionless concentration in the separator as a function of the concentrations at the edges of the separator. Because of continuity and what is assumed to be no uptake of solute into the filter paper, the concentrations from the liquid phase in one channel through the separator to the liquid phase in the connected channel must be continuous. Hence, the arguments of equation (17) are going to come from the concentrations obtained from solving the reaction diffusion equation in the liquid phases.

The Liquid Phases

The material balance and net flux can be expressed by equations (18) and (19).

$$\frac{\partial c_A}{\partial t} = -\nabla \cdot N_A + R_A \tag{18}$$

$$N_A = -D_A \nabla c_A \tag{19}$$

Assuming a steady state model with a constant diffusion coefficient and homogeneous reaction through the liquid phase.

$$0 = \frac{\partial^2 c_A}{\partial x^2} + \frac{R_A}{D_A} \tag{20}$$

$$\frac{\partial^2 c_A}{\partial x^2} = \frac{-R_A}{D_A}. \tag{21}$$

The two boundary conditions can be expressed as at

$$x = -L \tag{22}$$

$$\nabla c = 0 \tag{23}$$

$$x = 0 \tag{24}$$

$$c = \frac{c_{A,i}}{2} \tag{25}$$

Let the following non-dimensionalized parameters be expressed as

$$\overline{x} = \frac{x}{L} \tag{26}$$

$$\theta = \frac{c_A}{c_{A,i}} \tag{27}$$

Non-dimensionalizing the reaction diffusion equation leads to

$$\frac{\partial^2\theta}{\partial\overline{x}^2} = -\frac{w_{ch}^2 R_A}{c_{A,i} D} = \Psi \tag{28}$$

And non-dimensionalizing the first boundary condition leads to

$$\overline{x} = -1 \tag{29}$$

$$\nabla\theta = 0 \tag{30}$$

And non-dimensionalizing the second boundary condition leads to

$$\overline{x} = 0 \tag{31}$$

$$\theta = \frac{1}{2} \tag{32}$$

Integrating the non-dimensionalized reaction diffusion equation leads to the following expression

$$\theta = \frac{\Psi\overline{x}^2}{2} + k_1\overline{x} + k_2 \tag{33}$$

where k_1 and k_2 are integration constants. The boundary conditions must be applied separately. That is, for

$$\overline{x} < 0 \tag{34}$$

$$\theta_{x<0} = \frac{\Psi\overline{x}^2}{2} + \Psi\overline{x} + 1 \tag{35}$$

and similarly for

$$\bar{x} \geq 0 \tag{36}$$

$$\theta_{x\geq 0} = \frac{\Psi \bar{x}^2}{2} + \Psi \bar{x} + 1 \tag{37}$$

The equations, (35) and (37), are used to model the behavior of the transporting species in the liquid based on diffusion only occurring. Plotting the equations for constant values of Ψ along the dimensionless length of the reactor, in conjunction with the separator phase concentration equation, one can find the maximum value of Ψ that can be used to represent the reaction rate, as shown in Figure 32.

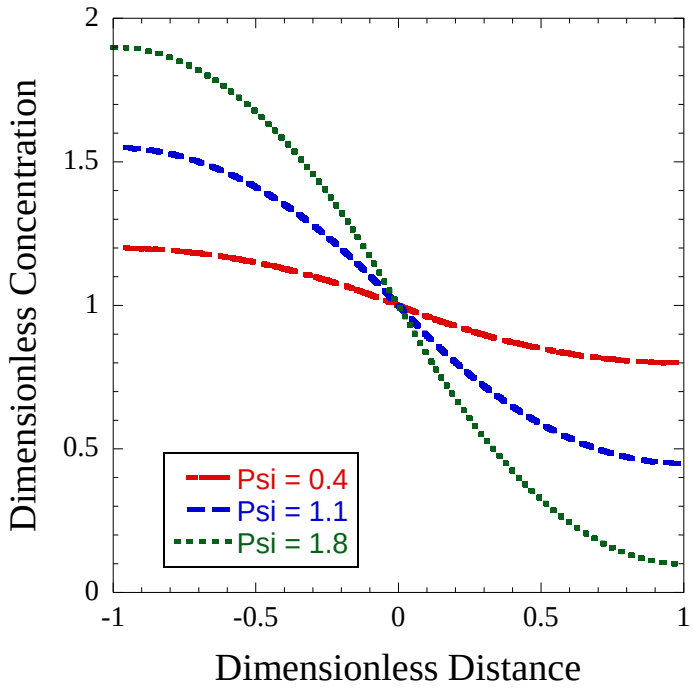

Figure 32. Dimensionless concentration as a function of dimensionless distance along the length of the reactor. Plot includes both liquid phases and separator phase concentration profiles.

The maximum value that is achievable is $\Psi = 1.8$ based on the requirement that $c_A \geq 0.1$. Ψ is then related back to the length of the reactor by

$$\Psi = -\frac{w_{ch}^2 R_A}{c_{A,i} D_A} \tag{38}$$

and then can be rearranged, neglecting the whether the reaction is producing or consuming A, to express the channel width as a function of Ψ,

$$w_{ch}^2 = \frac{\Psi c_{A,i} D_A}{R_A} \tag{39}$$

Table 18. Model parameters and results.

Parameter	Value	Units
$c_{A,i}$	1000	M
D_A	10^{-9}	$m^2 \times s^{-1}$
R_A	0.00421	$mol \times m^{-3} \times s^{-1}$
w_{ch}	20.7	mm

The results of the model suggest that the maximum channel width is around 20.7 mm, with respect to the other input parameters. This result suggests that for the input parameters shown, A is exhausted by the point the channel reached 20.7 mm in width. This means that for any channel width over 20.7 mm, the reactor is oversized, and any size larger than the maximum size means unused reactor space. Assuming a 1000 $kg \times day^{-1}$ production rate of hydrogen gas

[13], an approximate calculation of the reactor length shows that the reactor length required is unreasonably long. That is,

$$P_{H_2} = R_{H_2} V_{ch} t \tag{40}$$

where P_{H_2} is the daily production rate of hydrogen, at 1000 kg×day^{-1}, R_{H_2} is the rate constant at which hydrogen is formed (previously given), V_{ch} is the volume of the channel, and t is the time in seconds over which the reactor runs, which would be equivalent to twenty-four hours. Because the channel width, 20.7 mm, and the channel depth, 10 cm are known, the length of the channel is determined to be

$$L_{ch} = \frac{P_{H_2}}{d_{ch} w_{ch} R_{H_2} t}. \tag{41}$$

Solving for L_{ch} gives an approximate channel length of 664 km, assuming a 1000 kg×day^{-1} production rate. The material costs resulting from building excessively thin and long reactors like the one that the model suggests are likely to be higher than building a wider, less long reactor. In order to reduce the length assuming the daily production target, either the channel width or the channel depth need to be increased. Because the channel depth is fixed by the optimal penetration depth of sunlight, the channel width is determined to be the only parameter that can be increased.

APPENDIX B

BUCKINGHAM π THEOREM

In order to form a correlation, also known as the dimensionless mass-transfer coefficient, the Sherwood number, a dimensional analysis is required and can be done using the Buckingham π theorem [50]. Table 19 includes the parameters of interest in the system. The parameters are not an exhaustive list. Rather, they are chosen to best represent the system, based on intuition on the process. That is, this method is not based on scientific principle but still serves as an effective tool in developing a correlation.

Table 19. List of Variables for Buckingham π.

Variable Group	Physical Variable Name	Symbol	Dimensions
1	Diffusivity	D	$L^2 \times t^{-1}$
2	Channel Width	w_{ch}	L
3	Density Difference between Liquid and Gas	$\Delta\rho = (\rho_l - \rho_g)$	$M \times L^3$
	Liquid Density	ρ_l	$M \times L^3$
	Gas Density	ρ_g	$M \times L^3$
4	Mass-Transfer Coefficient	k_{ch}	$L \times t^{-1}$
5	Liquid Viscosity	μ	$M \times (Lt)^{-1}$
6	Gravity	g	$L \times t^{-2}$
7	Orifice Diameter	d_o	L
8	Gas Velocity	v_g	$L \times t^{-1}$
9	Superficial Gas Velocity	v_{sg}	$L \times t^{-1}$

The commonality amongst these parameters is their ability to be measured. The nine parameters are listed, along with their numbering, in the left most columns of the table. Their symbols are listed in the third column, along with their physical dimensions in the fourth column.

Table 20. Appendix physical variables and dimensions.

Dimensions	Physical Variable								
	D	w_{ch}	ρ_l, ρ_g, $\Delta\rho$	k_{ch}	μ	g	d_o	v_g	v_{sg}
M	0	0	1	0	1	0	0	0	0
L	2	1	-3	1	-1	1	1	1	1
t	-1	0	0	1	-1	-2	0	1	1

shows how the physical variables relate to the independent physical dimensions in the system, where 'M' represents mass, 'L' represents length, and 't' represents time. These core, physically independent dimensions, are assigned a specific numerical value to the physical variable based on the dimensions shown in Table 20. For example, because diffusivity has dimensions of squared length per unit time, and no physical dependence on mass, the diffusivity column in Table 20, contains zero units for mass, two units for length, and negative one units for time. Values that are negative represent values found in the denominator.

After determining the dimensions of the physical variables, the number of dimensionless groups is determined to be the remainder of the difference between the number of variables and the dimensional matrix. This value is often referred to as 'π' [32].

$$\text{Dimensionless Groups} = \text{Number of Variables} - \text{Rank of Dimensional Matrix} \tag{1}$$

$$\pi = n - r \tag{2}$$

$$6 = 9 - 3 \tag{3}$$

$$\therefore 1 = f(\pi_1\pi_2\pi_3\pi_4\pi_5\pi_6) \tag{4}$$

The four expected dimensionless groups are defined in equations (5) through (8).

$$\mathrm{Ar}^* = \frac{\Delta\rho^2 d_o^3 g}{\mu^2 \varepsilon} \tag{5}$$

$$\mathrm{Sh} = \frac{k_{ch} w_{ch}}{D} \tag{6}$$

$$\mathrm{Sc} = \frac{\mu}{\rho_l D} \tag{7}$$

$$\mathrm{Re} = \frac{\Delta\rho_l v_{sg} d_o}{\mu} \tag{8}$$

The selected core variables to be apart of each dimensionless group are

$$D, w_{ch}, \Delta\rho\,. \tag{9}$$

The six variables to be used to compose each of the six dimensionless groups are

$$k_{ch}, \mu, g, d_o, v_g, v_{sg}\,. \tag{10}$$

The following expressions are used to determine dimensionless group one.

$$\pi_1 = D^a w_{ch}^b \Delta\rho^c k_{ch} \tag{11}$$

$$M^0 L^0 t^0 = \left(\frac{L^2}{t}\right)^a (L)^b \left(\frac{M}{L^3}\right)^c \left(\frac{L}{t}\right) \tag{12}$$

$$\text{M: } 0 = c \tag{13}$$

$$\text{L: } 0 = 2a + b - 3c + 1 \tag{14}$$

$$\text{t: } 0 = -a - 1 \tag{15}$$

$$a = -1 \tag{16}$$

$$b = 1 \tag{17}$$

$$c = 0 \tag{18}$$

$$\pi_1 = \frac{k_{ch} w_{ch}}{D} = \text{Sh} \tag{19}$$

The following expressions are used to determine dimensionless group two.

$$\pi_2 = D^a w_{ch}^b \Delta\rho^c \mu \tag{20}$$

$$M^0 L^0 t^0 = \left(\frac{L^2}{t}\right)^a (L)^b \left(\frac{M}{L^3}\right)^c \left(\frac{M}{L \bullet t}\right) \tag{21}$$

$$\text{M: } 0 = c + 1 \tag{22}$$

$$\text{L: } 0 = 2a + b - 3c - 1 \tag{23}$$

$$\text{t: } 0 = -a - 1 \tag{24}$$

$$a = 1 \tag{25}$$

$$b = 0 \tag{26}$$

$$c = -1 \tag{27}$$

$$\pi_2 = \frac{\mu}{D\Delta\rho} = \mathrm{Sc} \tag{28}$$

$$\pi_2^{'} = \frac{D\Delta\rho}{\mu} = \mathrm{Sc}^{-1} \tag{29}$$

The following expressions are used to determine dimensionless group three.

$$\pi_3 = D^a w_{ch}^b \Delta\rho^c g \tag{30}$$

$$M^0 L^0 t^0 = \left(\frac{L^2}{t}\right)^a (L)^b \left(\frac{M}{L^3}\right)^c \left(\frac{L}{t^2}\right) \tag{31}$$

$$\mathrm{M:}\ 0 = c \tag{32}$$

$$\mathrm{L:}\ 0 = 2a + b - 3c + 1 \tag{33}$$

$$\mathrm{t:}\ 0 = -a - 2 \tag{34}$$

$$a = -2 \tag{35}$$

$$b = 3 \tag{36}$$

$$c = 0 \tag{37}$$

$$\pi_3 = \frac{w_{ch}^3 g}{D^2} \tag{38}$$

The following expressions are used to determine dimensionless group four.

$$\pi_4 = D^a w_{ch}^b \Delta\rho^c d_o \tag{39}$$

$$M^0 L^0 t^0 = \left(\frac{L^2}{t}\right)^a (L)^b \left(\frac{M}{L^3}\right)^c \left(\frac{L}{t}\right) \tag{40}$$

$$\text{M: } 0 = c \tag{41}$$

$$\text{L: } 0 = 2a + b - 3c + 1 \tag{42}$$

$$\text{t: } 0 = -a \tag{43}$$

$$a = 0 \tag{44}$$

$$b = -1 \tag{45}$$

$$c = 0 \tag{46}$$

$$\pi_4 = \frac{d_o}{w_{ch}} \tag{47}$$

The following expressions are used to determine dimensionless group five.

$$\pi_5 = D^a w_{ch}^b \Delta\rho^c v_g \tag{48}$$

$$M^0 L^0 t^0 = \left(\frac{L^2}{t}\right)^a (L)^b \left(\frac{M}{L^3}\right)^c \left(\frac{L}{t}\right) \tag{49}$$

$$\text{M: } 0 = c \tag{50}$$

$$\text{L: } 0 = 2a + b - 3c + 1 \tag{51}$$

$$\text{t: } 0 = -a - 1 \tag{52}$$

$$a = -1 \tag{53}$$

$$b = 1 \tag{54}$$

$$c = 0 \tag{55}$$

$$\pi_5 = \frac{w_{ch} v_g}{D} \tag{56}$$

And if

$$v_g = \frac{v_{sg}}{\varepsilon} \tag{57}$$

So that

$$\pi_5 = \frac{w_{ch} v_{sg}}{D\varepsilon} \tag{58}$$

The following expressions are used to determine dimensionless group six.

$$\pi_6 = D^a w_{ch}^b \Delta\rho^c v_{sg} \tag{59}$$

$$M^0 L^0 t^0 = \left(\frac{L^2}{t}\right)^a (L)^b \left(\frac{M}{L^3}\right)^c \left(\frac{L}{t}\right) \tag{60}$$

$$0 = c \tag{61}$$

$$0 = 2a + b - 3c + 1 \tag{62}$$

$$0 = -a - 1 \tag{63}$$

$$a = -1 \tag{64}$$

$$b = 1 \tag{65}$$

$$c = 0 \tag{66}$$

$$\pi_6 = \frac{w_{ch} v_{sg}}{D} \tag{67}$$

$$\pi_6^{'} = \frac{\pi_6}{\pi_5} = \varepsilon \tag{68}$$

The following expressions are used to revise dimensionless group three to better express the group in terms of a commonly used dimensionless group.

$$\pi_3 = \frac{w_{ch}^3 g}{D^2} \tag{69}$$

$$\pi_3^{'} = \pi_3 \times \pi_2^{'2} \times \pi_4^3 \times \pi_6^{-1} = \frac{d_o^3 g \Delta\rho^2}{\varepsilon \mu^2} = \mathrm{Ar}^* \tag{70}$$

The following expressions are used to revise dimensionless group five to better express the group in terms of a commonly used dimensionless group.

$$\pi_5 = \frac{w_{ch} v_g}{D} \tag{71}$$

$$\pi_5^{'} = \frac{w_{ch} v_g}{D} \times \pi_2^{'} \times \pi_4 \tag{72}$$

$$\pi_5^{'} = \frac{\Delta\rho v_g d_o}{\mu}\pi_6^{'} = \mathrm{Re} \tag{73}$$

$$\mathrm{Sh} = f(\pi_2, \pi_3^{'}, \pi_4, \pi_5^{'}, \pi_6^{'}) \tag{74}$$

$$\mathrm{Sh} = f(\mathrm{Re}, \mathrm{Ar}^{*}, \mathrm{Sc}, \frac{d_o}{w_{ch}}, \varepsilon) \tag{75}$$

Equation (75) is the final functional form of the correlation determined by using the Buckingham π theorem. As derived, the functional form of this dimensionless mass-transfer correlation assumes information about the system geometry. Despite the length of the channels being an obvious measureable parameter, it does not appear in the functional form of the expression. This is because the direction of concern is transport occurring orthogonally to the lateral direction, effectively the length of the channel; that is, transport that is occurring from one liquid phase through the membrane, to the second liquid phase. The length of the channel is also neglected from the function because of the design criteria. Effectively, the aspect ratio of the system is such that transport in the lateral direction does not help in the design because the reaction that occurs happens from channel to channel.

If an alternative system geometry is used, then the correlation is functionally dependent of that geometry. For example, if cells were to include impellers for mechanical mixing purposes, then references to orifice diameters would be unnecessary, as the primary method of mixing would be from mechanical agitation. As another example, if cells were interconnected with several separators in between liquid phases, and some liquid phases had no sparging while others made use of sparging, then using the correlation developed here would introduce significant error.

APPENDIX C

DERIVATION OF MASS-TRANSFER COEFFICIENT FITTING EQUATION

In the diffusion cell experiments, reactant diffuses across a phase boundary, that phase boundary being the filter paper separator. The channels, which contain liquid and electrolyte, are assumed to be well mixed in their bulk phases. This well mixed assumption is due to the sparging action that occurs in the channels. Because of this mixing, the only appreciable change in concentrations occurs close to the filter paper separator. And, as analogously seen in diffusion models of mass transfer, the driving force for mass transfer in these well mixed systems are the concentration differences in the bulk phases. Effectively, the mass flux is proportional to the concentration differences in the channels. Because the flux is proportional to the concentration difference, a proportionality constant is required to relate the two. In this case, K_{ov} represents that constant, which is also known as the overall mass-transfer coefficient. Because this method combines multiple phases and boundaries, it is commonly referred to as a lumped parameter model [32].

A transient, overall mass balance contains the proportionality constant, K_{ov}. In order to determine K_{ov} from the equation, parameter fitting is required. As Keil et al. note, the mass-transfer coefficient obtained from this well mixed liquid phase model is primarily applicable for this system geometry. The system geometry includes the aspect ratio of the system, the geometry of the sparging tubes, the orifice spacing, and a viscous liquid with similar properties to water [19].

In equation (1), K_{ov} is multiplied by the concentration differences in the bulk solution to obtain a total molar flux. These concentrations, c_1 and c_2 are both measureable, bulk concentrations in each of the channels. V_1 and V_2 are defined as the volume of the channels and $V_{1,i}$ is the volume of that channel at initial time. With that,

$$V_2 \frac{dc_2(t)}{dt} = K_{ov}(c_1(t) - c_2(t)) \tag{1}$$

and

$$c_1(t)V_1 + c_2(t)V_2 = c_{1,i}V_{1,i}\,. \tag{2}$$

Because the volumes of each of the channels are the same in the experimental apparatus, the assumption that

$$V_1 = V_2 = V_{1,i} \tag{3}$$

holds true. As a result, because the volumes are the same, equation (2) can be rewritten to show that the sum of the concentrations is equivalent to the initial concentration

$$c_1(t) + c_2(t) = c_{1,i}\,. \tag{4}$$

Furthermore, the model to determine the mass-transfer coefficient from the concentration versus time data is derived below after substituting equation (4) into (1).

$$V_2 \frac{dc_2(t)}{dt} = K_{ov}(c_{1,i} - c_2(t) - c_2(t)) = K_{ov}(c_{1,i} - 2c_2(t)) \tag{5}$$

$$\frac{dc_2(t)}{c_{1,i} - 2c_2(t)} = \frac{K_{ov}}{V_2} dt \tag{6}$$

Using integration by substitution with the following substitution constants,

$$u = c_{1,i} - 2c_2(t) \tag{7}$$

$$du = -2dc_2(t) \tag{8}$$

$$-\frac{1}{2} du = dc_2(t) \tag{9}$$

one can substitute into equation (6).

$$-\frac{du}{2u} = \frac{K_{ov}}{V_2} dt \tag{10}$$

Integrating equation (10) leads to the following expression, where G represents the constant upon integration of the expression.

$$\ln|u| = \frac{-2K_{ov}}{V_2} t + G \tag{11}$$

$$\ln\left|c_{1,i} - 2c_2(t)\right| = \frac{-2K_{ov}}{V_2} t + G \tag{12}$$

For the initial condition, at $t = 0$, the concentration in the second channel is zero; that is, $c_2 = 0$. This initial condition leads to the following expression.

$$\ln\left|c_{1,i}\right| = G \tag{13}$$

And substituting into equation (11), one arrives at the following expression:

$$\ln\left|c_{1,i} - 2c_2(t)\right| - \ln\left|c_{1,i}\right| = \frac{-2K_{ov}}{V_2}t \tag{14}$$

$$\ln\left|\frac{c_{1,i} - 2c_2(t)}{c_{1,i}}\right| = \frac{-2K_{ov}}{V_2}t \tag{15}$$

Taking the exponential of both sides leads to the following expression.

$$c_{1,i} - 2c_2(t) = c_{1,i}\exp(\frac{-2K_{ov}}{V_2}t) \tag{16}$$

$$-2c_2(t) = -c_{1,i} + c_{i,1}\exp(\frac{-2K_{ov}}{V_2}t) \tag{17}$$

$$c_2(t) = \frac{1}{2}(c_{1,i} - c_{1,i}\exp(\frac{-2K_{ov}}{V_2}t)) \tag{18}$$

$$c_2(t) = \frac{c_{1,i}}{2}(1 - \exp(\frac{-2K_{ov}}{V_2}t)) \tag{19}$$

The units of K_{ov} are cubic meters per second in the current form. However, if the cross sectional area through which diffusion occurs is introduced into the model, then the expression can be rewritten as

$$c_2(t) = \frac{c_{1,i}}{2}(1 - \exp(\frac{-2K_{ov}A_c}{V_2}t)) . \quad (20)$$

The cross sectional area, A_c, represents the area of the filter paper. The volume, V_2, is of either channel based on the assumptions in the model. Time, t, is the independent variable in the system. The initial concentration, $c_{1,i}$, can be rewritten to represent the total amount of mass transferred.

An equation with an exponential decay term as seen here is expected in this type of the physical system. The concentrations in both cells approach one another logarithmically. That is the only linearly sloped region in the experiment is at early times. As the concentration in the cell from which diffusion occurs decreases, the concentration in the diffused cell fast approaches nonlinearly. Additionally, as $t \to \infty$, the concentration in the channel approaches the equilibrium concentration, that being where the gradient in chemical potential is zero. This equilibrium concentration is intuitively half of the total initial concentration.

APPENDIX D

LUMPED PARAMETER MODEL SOLUTION

Several assumptions are used in the development of the well-mixed liquid phase mass transfer model, otherwise known as the lumped parameter model [32].

1. A thin film assumption is applied to the filter paper separator and independently in the channels. This means that the concentration profile through the separating phase and in the channels is linear.
2. No equilibrium partition coefficient is required as the solubility within the membrane phase is negligible.
3. The solutions on both sides of the separator are well mixed.
4. In the specific case that the resistances on both sides of the separator are the same, this implies that the mass-transfer coefficients, $k_{L,i} = k_{R,i}$. This assumption is valid when both channels operate at conditions that are identical.

The thin film assumption is used in this system for primarily two reasons. First, by using a filter paper separator, the resistance measurements in the separator phase are intended to be as small as compared to the liquid phase resistances as possible. Hence, a linear concentration profile with no solute uptake is to be desired. Second, and in result, one can expect no equilibrium partitioning to occur at the filter paper, liquid interface. Additionally, the flux is solely expected to be proportional to the concentration gradient. These two reasons are characteristics of the thin film model [32].

Of importance to note is that, in using the thin film assumption, an effective diffusivity, D_{eff}, for mass transport through the filter paper is required. Hence, the straightforward derivation shown below is useful in helping determine D_{eff}. If the resistances are identified and written in terms of their respective phases, then, certain sets of experiments can be done to identify diffusivities in each phase.

The first step in obtaining an expression for the overall mass-transfer coefficient, $K_{ov,i}$, is formulating overall mass balances for each species, i.

$$N_i = k_{L,i}(c_{LB,i} - c^*_{L,i}) \tag{1}$$

$$N_i = k_{R,i}(c^*_{R,i} - c_{RB,i}) \tag{2}$$

$$N_i = -D_i \nabla c_i = -D_i \frac{\Delta c_i}{\Delta x} = D_i \frac{\Delta(c^*_{L,i} - c^*_{R,i})}{x_{R,i} - x_{L,i}} \tag{3}$$

The flux across the interfaces, where the stagnant films and membrane meet in the channel, is constant in a steady state. Applying this reasoning for each species results in obtaining $K_{ov,i}$.

$$\frac{N_i}{k_{L,i}} = c_{LB,i} - c^*_{L,i} \tag{4}$$

$$\frac{N_i}{k_{R,i}} = c^*_{R,i} - c_{RB,i} \tag{5}$$

$$\frac{N_i}{k_{M,i}} = c^*_{L,i} - c^*_{R,i} \tag{6}$$

$$\frac{N_i}{k_{L,i}} + \frac{N_i}{k_{M,i}} + \frac{N_i}{k_{R,i}} = c_{LB,i} - c^*_{L,i} + c^*_{R,i} - c_{RB,i} + c^*_{L,i} - c^*_{R,i} \tag{7}$$

Knowing that the resistances are series resistances leads to the following expressions:

$$N_i \left(\frac{1}{k_{L,i}} + \frac{1}{k_{M,i}} + \frac{1}{k_{R,i}} \right) = c_{LB,i} - c_{RB,i} \tag{8}$$

Expressing (8) in terms of $K_{ov,i}$

$$\frac{1}{k_{L,i}} + \frac{1}{k_{M,i}} + \frac{1}{k_{R,i}} = \frac{1}{K_{ov,i}} \tag{9}$$

Equation (9) expresses the mass-transfer coefficient in terms of individual resistances through the diffusion cell. Other interesting Equation (9) allows the flux to be expressed in a driving force-resistance form,

$$N_i = \frac{c_{LB,i} - c_{RB,i}}{\frac{1}{K_{ov,i}}} \tag{10}$$

Or expressing the flux of species i in a convective mass transfer form,

$$N_i = K_{ov,i} \left(c_{LB,i} - c_{RB,i} \right) \tag{11}$$

The overall flux of each species can be obtained from equation (11).

The Effective Diffusivity, D_{eff}

D_{eff} is needed to determine the filter paper resistance. D_{eff} incorporates porosity and tortuosity effects on the aqueous diffusion coefficient. Diffusion coefficients of electrolytes in filter paper have been reported by Hashitani [51]. The D_{eff} 's reported are those for Millipore™ Filter Paper. For example, the D_{eff} for NH_4Cl at 25 °C for Millipore™ Filter Paper, 160 µm thickness, is reported to be $1.858\times10^{-9}\,m^2\times s^{-1}$. From the effective diffusivity, one can obtain a porosity-tortuosity correction. This correction is found to be 0.93. This correction can be applied to the aqueous diffusivity of KCl and is found to give an effective diffusivity of $1.84\times10^{-9}\,m^2\times s^{-1}$, for KCl in filter paper. By determining the effective diffusivity through the filter paper, it is possible to determine the resistance through the filter paper. The resistance is expressed as

$$\frac{1}{k_{M,i}} = \frac{\delta}{D_{eff,i}} \tag{12}$$

where δ is the thickness of the filter paper.

REFERENCES

1. Lee, R., *The Outlook for Population Growth.* Science, 2011. **333**(6042): p. 569-573.

2. Chu, S. and A. Majumdar, *Opportunities and challenges for a sustainable energy future.* Nature, 2012. **488**(7411): p. 294-303.

3. Lewis, N.S. and D.G. Nocera, *Powering the planet: Chemical challenges in solar energy utilization.* Proceedings of the National Academy of Sciences, 2006. **103**(43): p. 15729-15735.

4. Hill, J., et al., *Environmental, economic, and energetic costs and benefits of biodiesel and ethanol biofuels.* Proceedings of the National Academy of Sciences of the United States of America, 2006. **103**(30): p. 11206-11210.

5. Scrosati, B. and J. Garche, *Lithium batteries: Status, prospects and future.* Journal of Power Sources, 2010. **195**(9): p. 2419-2430.

6. Steele, B.C.H. and A. Heinzel, *Materials for fuel-cell technologies.* Nature, 2001. **414**(6861): p. 345-352.

7. Carrasco, J.M., et al., *Power-electronic systems for the grid integration of renewable energy sources: A survey.* Ieee Transactions on Industrial Electronics, 2006. **53**(4): p. 1002-1016.

8. Archer, M.D., *Photovoltaics and photoelectrochemistry: similarities and differences.* Physica E-Low-Dimensional Systems & Nanostructures, 2002. **14**(1-2): p. 61-64.

9. Kalogirou, S.A., *Solar thermal collectors and applications.* Progress in Energy and Combustion Science, 2004. **30**(3): p. 231-295.

10. Gratzel, M., *Photoelectrochemical cells.* Nature, 2001. **414**(6861): p. 338-344.

11. Gratzel, M., *Solar energy conversion by dye-sensitized photovoltaic cells.* Inorganic Chemistry, 2005. **44**(20): p. 6841-6851.

12. Peumans, P., A. Yakimov, and S.R. Forrest, *Small molecular weight organic thin-film photodetectors and solar cells.* Journal of Applied Physics, 2003. **93**(7): p. 3693-3723.

13. James, B.D., et al., *Technoeconomic analysis of photoelectrochemical (PEC) hydrogen production.* 2009.

14. Wolfbauer, G., et al., *A channel flow cell system specifically designed to test the efficiency of redox shuttles in dye sensitized solar cells.* Solar Energy Materials and Solar Cells, 2001. **70**(1): p. 85-101.

15. Boschloo, G. and A. Hagfeldt, *Characteristics of the Iodide/Triiodide Redox Mediator in Dye-Sensitized Solar Cells.* Accounts of Chemical Research, 2009. **42**(11): p. 1819-1826.

16. U.S. Department of Energy; Hydrogen, F.C.a.I.T.P., *Lower and Higher Heating Values of Fuels.*

17. Sedahmed, G.H., et al., *Effect of gas sparging on the rate of mass transfer during electropolishing of vertical plates.* Chemical Engineering and Processing: Process Intensification, 2001. **40**(3): p. 195-200.

18. Jenkins, S., *FACTS AT YOUR FINGERTIPS.* Chemical Engineering, 2012. **119**(9): p. 33-33.

19. Keil, Z.O. and T.W.F. Russell, *DESIGN OF COMMERICIAL-SCALE GAS-LIQUID CONTACTORS.* Aiche Journal, 1987. **33**(3): p. 488-496.

20. Botton, R., D. Cosserat, and J.C. Charpentier, *Operating zone and scale up of mechanically stirred gas-liquid reactors.* Chemical Engineering Science, 1980. **35**(1–2): p. 82-89.

21. Vogt, H., *THE ROLE OF SINGLE-PHASE FREE-CONVECTION IN MASS-TRANSFER AT GAS EVOLVING ELECTRODES .1. THEORETICAL.* Electrochimica Acta, 1993. **38**(10): p. 1421-1426.

22. Haque, M.W., K.D.P. Nigam, and J.B. Joshi, *OPTIMUM GAS SPARGER DESIGN FOR BUBBLE-COLUMNS WITH A LOW HEIGHT-TO-DIAMETER RATIO.* Chemical Engineering Journal and the Biochemical Engineering Journal, 1986. **33**(2): p. 63-69.

23. Cui, Z.F. and K.I.T. Wright, *FLUX ENHANCEMENTS WITH GAS SPARGING IN DOWNWARDS CROSSFLOW ULTRAFILTRATION: PERFORMANCE AND MECHANISM.* Journal of Membrane Science, 1996. **117**(1-2): p. 109-116.

24. Ettel, V.A., B.V. Tilak, and A.S. Gendron, *MEASUREMENT OF CATHODE MASS-TRANSFER COEFFICIENTS IN ELECTROWINNING CELLS.* Journal of the Electrochemical Society, 1974. **121**(7): p. 867-872.

25. Rigby, G.D., et al., *Gas bubble induced mixing in electrowinning baths.* Chemical Engineering Science, 2001. **56**(21–22): p. 6329-6336.

26. Tobias, C.W., M. Eisenberg, and C.R. Wilke, *DIFFUSION AND CONVECTION IN ELECTROLYSIS - A THEORETICAL REVIEW.* Journal of the Electrochemical Society, 1952. **99**(12): p. C359-C365.

27. Sigrist, L., O. Dossenbach, and N. Ibl, *MASS-TRANSPORT IN ELECTROLYTIC CELLS WITH GAS SPARGING.* International Journal of Heat and Mass Transfer, 1979. **22**(10): p. 1393-1399.

28. Miller, D.N., *SCALE-UP OF AGITATED VESSELS GAS-LIQUID MASS-TRANSFER.* Aiche Journal, 1974. **20**(3): p. 445-453.

29. Bredwell, M.D. and R.M. Worden, *Mass-transfer properties of microbubbles. 1. Experimental studies.* Biotechnology Progress, 1998. **14**(1): p. 31-38.

30. Prince, M.J. and H.W. Blanch, *BUBBLE COALESCENCE AND BREAK-UP IN AIR-SPARGED BUBBLE-COLUMNS.* Aiche Journal, 1990. **36**(10): p. 1485-1499.

31. Cabassud, C., et al., *Air sparging in ultrafiltration hollow fibers: relationship between flux enhancement, cake characteristics and hydrodynamic parameters.* Journal of Membrane Science, 2001. **181**(1): p. 57-69.

32. Cussler, E.L., *Diffusion, mass transfer in fluid systems*. 1984, Cambridge University Press: Cambridge Cambridgeshire ;.

33. Hines, A.L., *Mass transfer : fundamentals and applications*. Prentice-Hall international series in the physical and chemical engineering sciences, ed. R.N. Maddox. 1985, Prentice-Hall: Englewood Cliffs, N.J.

34. Welty, J.R., *Fundamentals of momentum, heat, and mass transfer*. 5th ed. ed. 2008, Wiley: Hoboken, N.J. ;.

35. Bird, R.B., *Transport phenomena*. 2nd ed. ed, ed. W.E. Stewart and E.N. Lightfoot. 2002, J. Wiley: New York.

36. Chao, K.P., S.K. Ong, and M.C. Huang, *Mass transfer of VOCs in laboratory-scale air sparging tank.* Journal of Hazardous Materials, 2008. **152**(3): p. 1098-1107.

37. Oguz, H. and A. Brehm, *MASS-TRANSFER COEFFICIENTS IN ORGANIC SLURRIES WITH MECHANICAL AGITATION AND SPARGING.* Chemical Engineering Science, 1988. **43**(6): p. 1416-1418.

38. Oguz, H., A. Brehm, and W.D. Deckwer, *GAS-LIQUID MASS-TRANSFER IN SPARGED AGITATED SLURRIES.* Chemical Engineering Science, 1987. **42**(7): p. 1815-1822.

39. Stephan, K. and H. Vogt, *MODEL FOR CORRELATING MASS-TRANSFER DATA AT GAS EVOLVING ELECTRODES.* Electrochimica Acta, 1979. **24**(1): p. 11-18.

40. Khamadieva, R. and U. Bohm, *Mass transfer to the wall of a packed and unpacked bubble column operating with Newtonian and non-Newtonian liquids.* Chemical Engineering Journal, 2006. **116**(2): p. 105-113.

41. Cui, Z.F., S. Chang, and A.G. Fane, *The use of gas bubbling to enhance membrane processes.* Journal of Membrane Science, 2003. **221**(1-2): p. 1-35.

42. Hosny, A.Y., et al., *EFFECT OF GAS SPARGING ON MASS-TRANSFER IN ZINC ELECTROLYTES.* Journal of Applied Electrochemistry, 1992. **22**(7): p. 596-605.

43. Vogt, H., *THE ROLE OF SINGLE-PHASE FREE-CONVECTION IN MASS-TRANSFER AT GAS EVOLVING ELECTRODES .2. EXPERIMENTAL-VERIFICATION.* Electrochimica Acta, 1993. **38**(10): p. 1427-1431.

44. Bhavaraju, S.M., T.W.F. Russell, and H.W. Blanch, *DESIGN OF GAS SPARGED DEVICES FOR VISCOUS-LIQUID SYSTEMS.* Aiche Journal, 1978. **24**(3): p. 454-465.

45. Kulkarni, A.A. and J.B. Joshi, *Bubble Formation and Bubble Rise Velocity in Gas−Liquid Systems: A Review.* Industrial & Engineering Chemistry Research, 2005. **44**(16): p. 5873-5931.

46. Li, Q.Y., Z.F. Cui, and D.S. Pepper, *Effect of bubble size and frequency on the permeate flux of gas sparged ultrafiltration with tubular membranes.* Chemical Engineering Journal, 1997. **67**(1): p. 71-75.

47. Lau, R., P.H.V. Lee, and T. Chen, *Mass transfer studies in shallow bubble column reactors.* Chemical Engineering and Processing: Process Intensification, 2012. **62**(0): p. 18-25.

48. Darrall, K.G. and G. Oldham, *The diffusion coefficients of the tri-iodide ion in aqueous solutions.* Journal of the Chemical Society A: Inorganic, Physical, Theoretical, 1968. **0**(0): p. 2584-2586.

49. Klein, S.A., *Engineering Equation Solver*. 2012.

50. Buckingham, E., *On Physically Similar Systems; Illustrations of the Use of Dimensional Equations.* Physical Review, 1914. **4**(4): p. 345-376.

51. Hashitani, T. and R. Tamamushi, *Rapid measurements of diffusion coefficients of electrolytes in aqueous solutions by the diaphragm-cell method.* Transactions of the Faraday Society, 1967. **63**(0): p. 369-371.